Hadron-production mechanisms in antineutrino-proton charged-current interactions

M. Derrick, P. Gregory,* F. LoPinto,† B. Musgrave, J. Schlereth, P. Schreiner, and R. Singer†
Argonne National Laboratory, Argonne, Illinois 60439

S. J. Barish,‡ R. Brock,§ A. Engler, T. Kikuchi, R. W. Kraemer, F. Messing, B. J. Stacey,¶ and M. Tabak**
Carnegie-Mellon University, Pittsburgh, Pennsylvania 15213

V. E. Barnes, D. D. Carmony, E. Fernandez,†† A. F. Garfinkel, and A. T. Laasanen
Purdue University, West Lafayette, Indiana 47907

(Received 28 January 1981)

In this paper we present results on hadronic production in antineutrino-proton interactions. The data sample, which consists of 2033 charged-current events with antineutrino energy above 5 GeV, comes from exposures of the 15-foot hydrogen bubble chamber to the Fermilab broad-band antineutrino beam. The results are discussed in terms of both their exclusive-channel components and the deep-inelastic part of the data, for which the total hadronic mass W and the lepton four-momentum transfer Q^2 are large. The current-quark fragmentation shows properties in good agreement with the simple quark-parton model. In particular, the data show no evidence for scaling violations or breakdown of the factorization hypothesis when the selections appropriate to obtaining the current-quark fragments are used. The jetlike features of the events and the energy and charge correlations in the quark fragmentation region are in reasonable agreement with the standard jet model of Field and Feynman. However, these features and the transverse-momentum properties of the current-quark fragments also follow phase-space predictions. The characteristics of the spectator-diquark (target fragmentation) system are presented. These features are compared to those of the current-quark system and to some predictions of quark-fusion models for proton fragmentation.

I. INTRODUCTION

The generally accepted framework for discussing the production of hadrons in such processes as

$$\bar{\nu}p \to \mu^+ + \text{hadrons} \tag{1}$$

is the quark-parton model (QPM).[1] In its simplest form, this model considers the charged-current reaction to be mediated by the exchange of a virtual boson W^-, which interacts with one of the quarks in the nucleon target. The transverse momentum of the quarks in the nucleon is neglected. Thus hadronic production through exclusive channels such as

$$\bar{\nu}p \to \mu^+\Delta^0 \to \mu^+ p\pi^- \tag{2}$$

involves a rearrangement of the quark configuration, transforming the nucleon to a $\Delta(1236)$. In a deep-inelastic interaction, the W^- strikes a valence u quark changing it to a d quark, which then fragments independently of the other quarks in the nucleon target to produce hadrons called the current-quark fragments,

$$W^- + u \to d \to \text{hadrons}. \tag{3}$$

The residual diquark, in this case a (ud) combination, acts as a spectator and itself breaks up into hadrons, the target fragments, as shown schematically in Fig. 1.

This simple parton model describes the main features of the existing data from leptoproduction reactions quite well.[2-7] The hadronic system resulting from quark fragmentation is generally independent of the production variables at the lepton vertex, as expected. However, with the recent availability of more precise data and the opportunity to explore higher values of the hadronic mass W and the lepton four-momentum transfer Q^2, some deviations are found. Modifications to the simple QPM are certainly expected from effects such as an intrinsic quark transverse momentum inside the nucleon, the collision of the

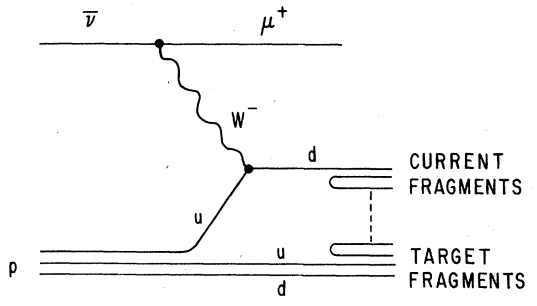

FIG. 1. Schematic representation of d-quark fragmentation following the interaction of a virtual W^- weak boson with a u quark from a proton target.

W^- boson with a gluon constituent, and gluon radiation by the struck quark. Such effects are predicted by quantum chromodynamics (QCD) to appear as scaling violations and nonfactorization in quark fragmentation functions and would result, for example, in a dependence of the hadron mean transverse momentum on Q^2 and W. Thus, a detailed study of the properties of hadrons produced in leptoproduction reactions is important in providing quantitative tests of this theory.

A striking feature of the hadronic system resulting from deep-inelastic quark transitions induced by hadron or lepton beams should be the presence of jets of hadrons. In both ν and $\bar{\nu}$ processes, the flavor of the struck quark is known, aside from small contributions from the nucleon sea. Thus neutrino probes present some advantages in studying such jet properties as leading-particle effects and momentum and charge correlations, as well as in comparing to models of quark hadronization. Moreover, particle production in $(\nu\bar{\nu})$-nucleon processes are related to those in (e,μ)-nucleon interactions, to e^+e^- annihilations and to high-transverse-momentum hadronic interactions through the QPM.[6,8] In the (e,μ)-nucleon interaction, the coupling goes via the quark charge, so that the u-quark fragmentation contributes $\frac{8}{9}$ of the cross section for a proton target. Thus, the characteristics of these reactions should be similar to the νp case. In e^+e^- annihilations, u, d, s, c, and b quarks all contribute, weighted by the square of the quark charge, once the appropriate threshold has been passed. So $\bar{\nu}p$ reactions provide a unique tool for studying d-quark fragmentation.

The data presented in this paper come from a bubble-chamber experiment which provides the advantages of complete kinematical coverage and some neutral-particle detection but also suffers the drawbacks of limited charged-hadron identification and statistical precision. In contrast, the experiments using charged-lepton beams generally have good statistical precision and particle identification, but have restricted kinematical coverage.[7,9] Nevertheless, it is important to compare the characteristics of the hadrons produced in these different processes in order to search for the regularities predicted by the QPM.

II. EXPERIMENTAL DETAILS

The data sample was obtained from three separate exposures of the Fermilab 15-foot hydrogen bubble chamber. Most of the 226 000 pictures were obtained with a 400-GeV proton beam and two focusing horns to provide a broad-band antineutrino beam. The neutrino background flux was at the 10% level except at the highest energies.[10]

The scanning process selected all events for which the total momentum in the forward hemisphere exceeded 2 GeV/c. Because of the difficulty in finding one-prong events, they are not in the data sample. Since this paper deals primarily with charged hadrons, this omission introduces no serious bias. All charged-current events containing a V^0 are included. The overall scanning and final average event reconstruction efficiencies were ~ 90 and 95%, respectively. Multiplicity-dependent corrections for scanning and measuring losses were applied.

The $\bar{\nu}p$ charged-current (CC) events are extracted from a raw sampling comprising contributions from both CC and neutral-current (NC) reactions

$$\bar{\nu}p \to \mu^+ H^0, \tag{4}$$

$$\nu p \to \mu^- H^{++}, \tag{5}$$

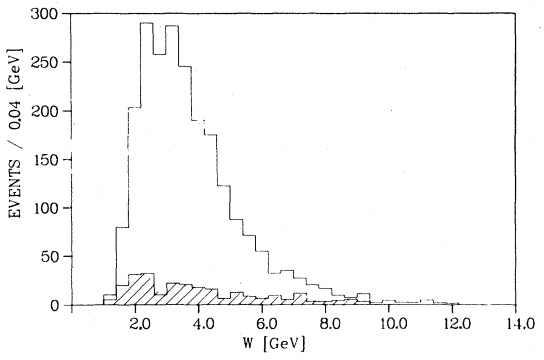

FIG. 2. The distribution in hadronic mass W for the system of charged hadrons in $\bar{\nu}p \to \mu^+ h^\pm X$ events. The event subsample, which is assigned as the $\mu^+ p\pi^-$ or $\mu^+ p\pi^-\pi^+\pi^-$ final states, is shown shaded.

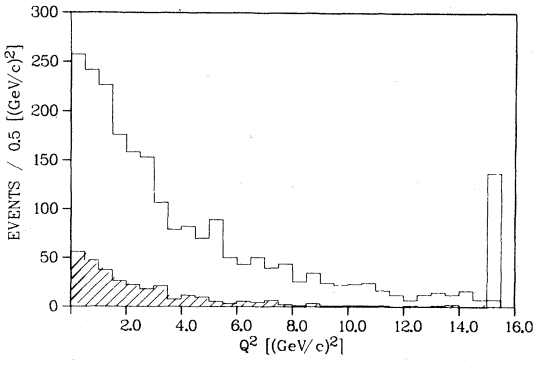

FIG. 3. The distribution in lepton four-momentum transfer, Q^2, in the $\bar{\nu}p \to \mu^+ h^\pm X$ events. The event subsample, which is assigned to the $\mu^+ p\pi^-$ or $\mu^+ p\pi^-\pi^+\pi^-$ final states, is shown shaded. The events with $Q^2 \geq 15$ (GeV/c)^2 are shown in an overflow bin.

$$\nu p \to \bar{\nu} H^+, \tag{6}$$

$$\nu p \to \nu H^+. \tag{7}$$

Backgrounds from K_L^0 mesons and neutrons are small and by requiring the charged tracks to have a total momentum ≥ 5 GeV/c can be ignored.[11]

Empirical muon-selection criteria for the separation of CC and NC events have been developed in a Monte Carlo simulation of the experiment.[10,12] Any track with $P_T < 1$ GeV/c relative to the beam and which had at least twice the momentum of any other track was called the muon. In events not satisfying this selection, the track with highest transverse momentum (P_T) relative to the total momentum vector of the remaining charged particles was called the muon, provided $P_T \geq 1.2$ GeV/c. Otherwise, the event was classified as a NC candidate.

The measurement of the beam energy for events with missing neutrals was made using a modification of a method due to Grant in which the energy is parametrized in terms of the transverse momentum of the missing-neutral system relative to the total-hadron direction. The antineutrino energy resolution, as calculated from the Monte Carlo simulation, is $\pm 9\%$. A further check on the technique is obtained by taking events with no neutral particles, such as the final states $\mu^+ p \pi^-$ and $\mu^+ p \pi^- \pi^+ \pi^-$ (identified by kinematical fitting) and computing the energy after deleting one or more hadrons. The resolution estimated in this way is $\pm 12.5\%$. The resolution in the total hadronic energy W is about three times worse than that for the antineutrino energy.

Results are given for three or more charged particles, and we apply the selection $0.1 < Y < 0.8$ throughout, where Y is the usual scaling variable. In general, no cut on the Bjorken variable X_{BJ} is made unless indicated. Hadrons with laboratory momentum less than 1 GeV/c, which are identified as protons by ionization density in the chamber, are called protons; all other charged hadrons are assigned the pion mass.

In order to present distributions where the effects of instrumental smearing from measurement uncertainties, muon selection and neutrino energy determination are minimized, we again employ

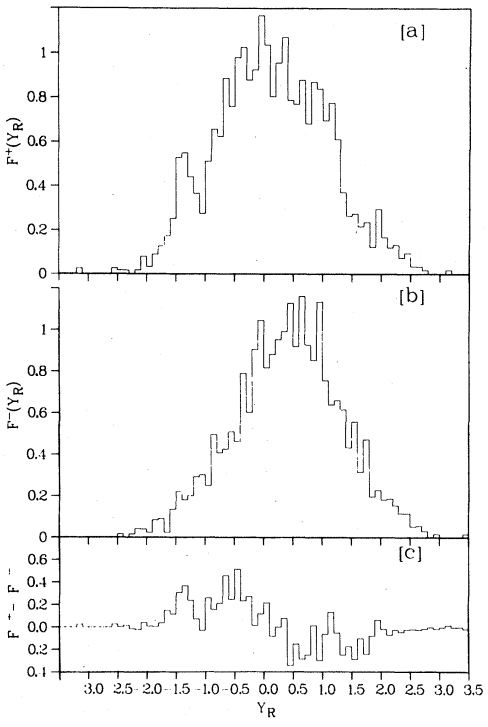

FIG. 4. The single-particle distribution in rapidity, Y_R, in the hadronic c.m. system for $\bar{\nu}p \to \mu^+ h^\pm X$ events with $W \geq 4$ GeV and $1.0 \leq Q^2 < 45$ (GeV/c)^2 for (a) positive hadrons and (b) negative hadrons. In (c), the net charge per event, defined as positive minus negative, is also shown as a function of Y_R. The peak near $Y_R = -1.5$ in (a) corresponds to the identified protons.

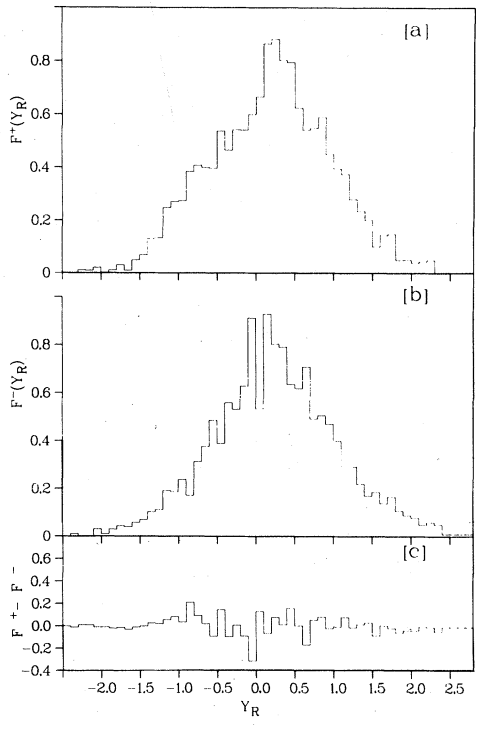

FIG. 5. The single-particle rapidity distributions in the hadronic c.m. system for $\bar{\nu}p \to \mu^+ h^\pm X$ events with $W < 4$ GeV and $1.0 \leq Q^2 < 45$ (GeV/c)^2 for (a) positive hadrons and (b) negative hadrons. In (c), the net charge per event, defined as positive minus negative, is also shown as a function of Y_R.

the Monte Carlo simulation of the experiment.[12] The program is run first with no measurement uncertainties on the tracks and with known muon identity and neutrino energy, and then it is run with these uncertainties included so as to simulate the experimental conditions. Comparison of the results from the two runs allows the correction function for a given variable to be derived. The program incorporates known data to specify the distributions in X_{BJ}, Y, and P_T of the secondary hadrons and the multiplicity distributions of charged and neutral secondaries. However, such details as jet and resonance production are not input to the program. The nucleons are generated according to the X_F distribution observed in the experiment. These corrections are generally smaller than 15% and, unless otherwise indicated, all distributions shown have been corrected.

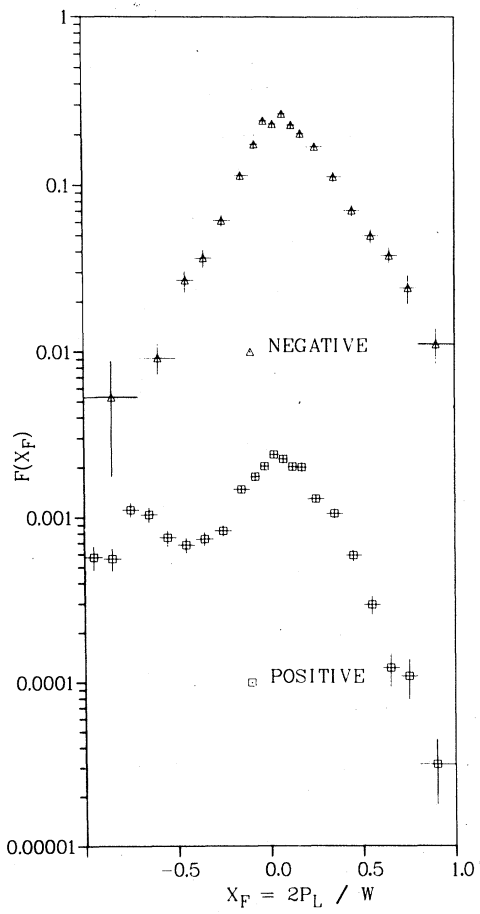

FIG. 6. Normalized Lorentz-invariant cross sections $F(X_F)$ for positive and negative hadrons in $\bar{\nu}p \to \mu^+ h^\pm X$ events. The ordinate scale applies to the negative distribution. The data points for positive hadrons are displaced down by two decades.

III. DEFINITION OF VARIABLES AND EVENT SAMPLES

We use the conventional deep-inelastic scattering variables $X_{BJ} = Q^2/2M\nu$ and $Y = \nu/E_{\bar{\nu}}$, where Q is the lepton four-momentum transfer, ν is the energy transfer between leptons, and M is the proton mass.

In the QPM, the cross section for the semi-inclusive reaction $\bar{\nu}p \to \mu^+ h^\pm X$ is expressed in terms of the elementary scattering of the exchanged current on a constituent quark (q') followed by the fragmentation of the produced quark (q) into hadrons (h), each of which takes a frac-

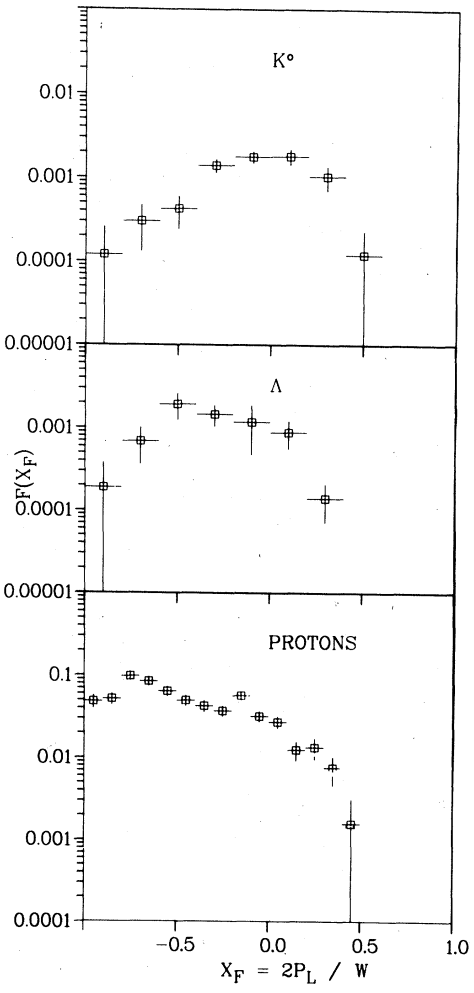

FIG. 7. Normalized Lorentz-invariant cross sections $F(X_F)$ for protons, Λ^0 hyperons, and K_S^0 mesons in $\bar{\nu}p \to \mu^+(p, \Lambda^0, K_S^0)X$ events. The neutral-particle cross sections include corrections for neutral decay modes. The protons have been identified either by visual inspection or by kinematical fitting.

tion Z of the quark energy:

$$\frac{d\sigma^h}{dX\,dY\,dZ} = \sum \left(\frac{d\sigma}{dX\,dY}\right)_{q'\to q} D_q^h(Z), \tag{8}$$

where the sum extends over the different quark flavors taking part. In the simplest model, the transverse momentum of quarks in the nucleon is ignored so that the fragmentation or D function, which gives the probability of a scattered quark to produce hadron h, is independent of transverse momentum. In $\bar{\nu}p$ reactions, the dominant Cabibbo-allowed quark transitions are $W^- + u \to d$ and $W^- + \bar{d} \to \bar{u}$. Our studies of the X_{BJ} distribution of the inclusive sample indicates that ~ 8% of the events come from $\bar{d} \to \bar{u}$ transitions.[13] The strangeness and charm-changing transitions ($u \to s$, $\bar{s} \to \bar{c}$) account for less than 10% of the cross section. The hadron-production cross section is expected to factorize with $D_q^h(Z)$ being independent of the production variables X_{BJ}, Y, Q^2, etc., provided that the observed hadrons are indeed only fragments of the struck quark.

At a given hadronic mass W and lepton four-momentum-transfer squared Q^2 the hadronic system occupies a rapidity range proportional to $\ln W^2$. The raw distributions in W and Q^2 for our charged-current data sample are shown in Figs. 2 and 3, respectively. The median value of W is 3.7 GeV, so that only a small interval of rapidity is available. As is well known,[2] the overall charged-hadron multiplicity shows little dependence on Q^2 but grows logarithmically with W.

The hadrons associated with the more easily identifiable constrained channels $\bar{\nu}p \to \mu^+ p\pi^-$ and $\bar{\nu}p \to \mu^+ p\pi^-\pi^+\pi^-$ tend to occur at the lower values of W and Q^2, as seen by the hatched areas in Figs. 2 and 3. This is expected since N^* and Δ production are important in these channels.[14]

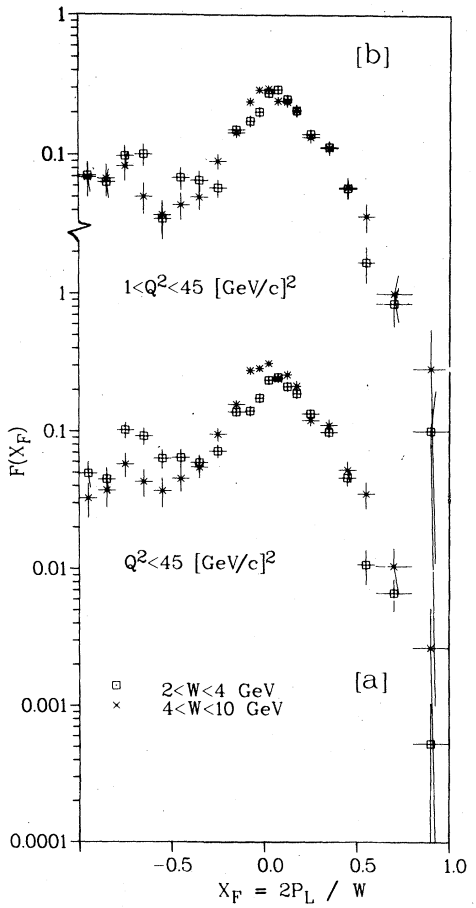

FIG. 8. Normalized Lorentz-invariant cross section $F(X_F)$ for positive hadrons in $\bar{\nu}p \to \mu^+ h^+ X$ events for the different selections on W and Q^2 shown. The ordinate scale applies to the lower set of data. The upper set of data is displaced upwards by two decades.

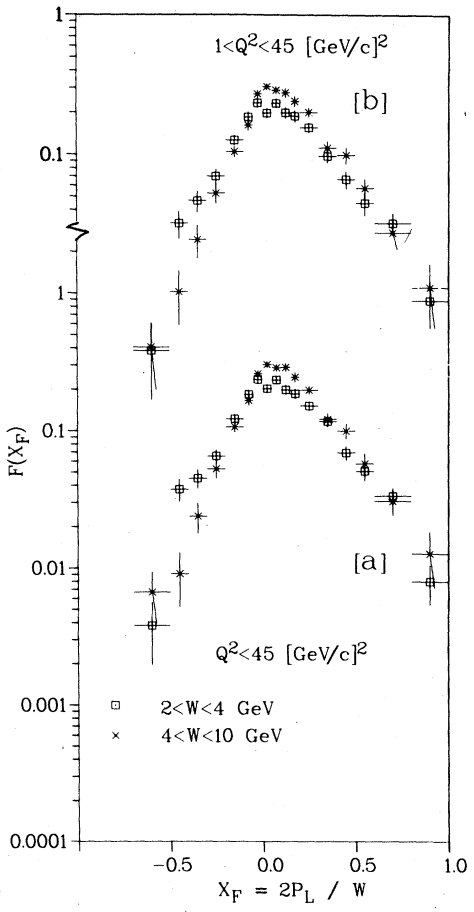

FIG. 9. Normalized Lorentz-invariant cross section $F(X_F)$ for negative hadrons in $\bar{\nu}p \to \mu^+ h^- X$ events for the different selections on W and Q^2 shown. The ordinate scale applies to the lower set of data. The upper set of data is displaced upwards by two decades.

The deep-inelastic events which contain the fragments of the current quark and the diquark system can, in principle, be selected by appropriate cuts on W and Q^2. A clean separation of the current quark and the target fragmentions, however, requires that each have available at least two units of rapidity, the value typical of rapidity correlations in hadron physics.[15] Such a separation begins to be possible for $W \geq 4$ GeV. This is illustrated in Fig. 4, where the distribution of rapidity, $Y_R = \frac{1}{2} \ln[(E^* + P_L^*)/(E^* - P_L^*)]$ in the hadronic center-of-mass (c.m.) system is shown for events with $W \geq 4$ GeV and $1 \leq Q^2 < 45$ (GeV/c)^2. The single-particle distributions, defined as

$$F(Y_R) = \frac{1}{N_{ev}} \frac{dN_h}{dY_T}, \tag{9}$$

are shown separately for positive and for negative hadrons in Figs. 4(a) and 4(b), respectively. We also show the difference between these distributions in Fig. 4(c). This difference measures the net charge as a function of rapidity. There is a net negative (positive) charge in the forward (backward) hemisphere which is the expected behavior.

At low W, $W < 4$ GeV, there is no evidence for a rapidity plateau and no clear separation of charge between forward and backward hemispheres seems possible as seen in the equivalent plots of Fig. 5.

The selections $W \geq 4$ GeV and $1 \leq Q^2 < 45$ (GeV/c)^2 are therefore applied as minimal requirements to separate current and target fragments. These kinematic selections also reduce the contamination from exclusive reactions. After these cuts, 566 (704.3) raw (weighted) events remain to study d-quark fragmentation. Since W and Q are related by the expression

$$W^2 = M^2 + Q^2\left(\frac{1}{X_{BJ}} - 1\right), \tag{10}$$

the W and Q^2 cuts effectively restrict $X_{BJ} \gtrsim 0.05$.

In studies of the properties of the current-quark fragments, we use the hadronic c.m. system and require also that Feynman X, $X_F = 2P_L^*/W \geq 0$. This definition is in accord with that used by other groups and so facilitates comparison with their results.[5] The energy fraction carried by any individual hadron is $Z_L = (\vec{p} \cdot \vec{h})/(\vec{p} \cdot \vec{q}) = E_{HAD}/\nu$ in terms of laboratory four-momenta p, h, and q for the target, hadron, and momentum transfer, respectively. In the limit of high energy, the fragmenting quark has energy $W/2$ in this frame. Occasionally, it will be useful to utilize the Breit frame in which the exchanged current has zero energy and where the struck quark has momentum $Q/2$. In this case, the momentum fraction is $Z_B = 2P_L^B/Q$, where P_L^B

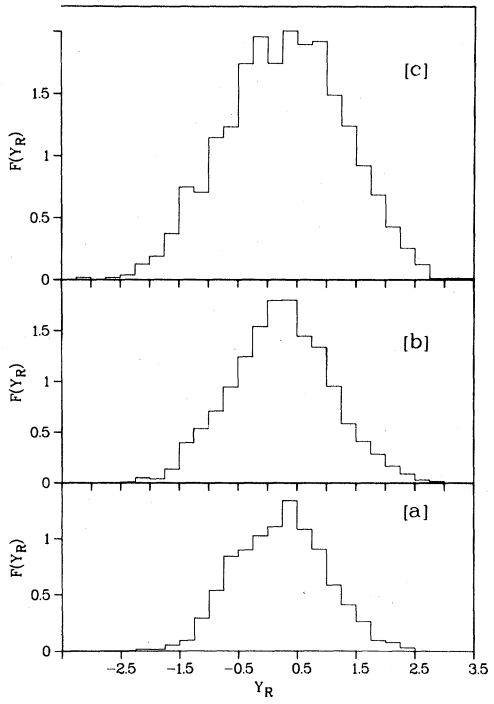

FIG. 10. The rapidity distribution $F(Y_R) = (1/N_{ev})dN_T/dY_R$ for all charged hadrons in $\bar{\nu}p \to \mu^+ h^\pm X$ events with $Q^2 < 45$ (GeV/c)^2 for (a) $1 \leq W < 3$ GeV, (b) $3 \leq W < 5$ GeV, and (c) $W \geq 5$ GeV.

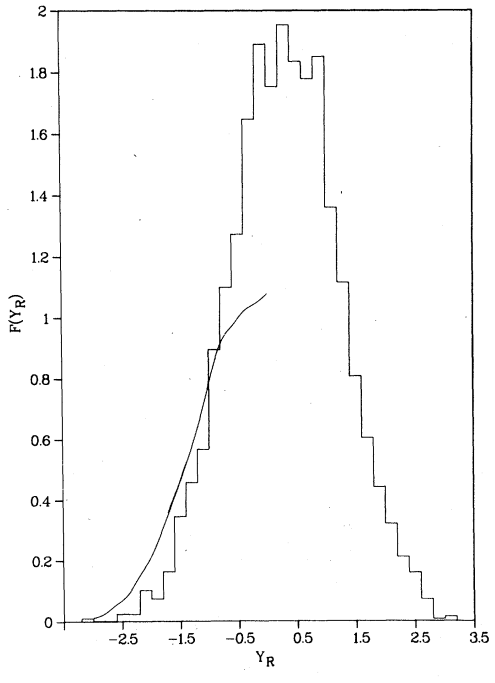

FIG. 11. The rapidity distribution $F(Y_R) = (1/N_{ev})dN_T/dY_R$ for all charged hadrons in $\bar{\nu}p \to \mu^+ h^\pm X$ events with $4 < W \leq 12$ GeV. Protons identified by ionization have been removed. The line shows the equivalent data for the hadronic reaction $pp \to \pi^\pm X$ at 24 GeV/c.

is the hadron momentum along the Q direction in the Breit frame. At the low energy of our experiment, the results are sometimes frame dependent.[16]

IV. INCLUSIVE DISTRIBUTIONS AND CHARGE SEPARATION

The normalized Lorentz-invariant cross section

$$F(X_F) = \frac{1}{\sigma}\frac{2}{\pi W}\int_0^\infty E^* \frac{d^2\sigma}{dX_F\, dP_T^2}\, dP_T^2 \qquad (11)$$

is shown in Fig. 6 for the complete data sample of 2567 events separately for positive and for negative hadrons. These distributions also exhibit the asymmetry observed in the exchanged-particle–target rest frame for other lepton- and hadron-induced processes.[17] The invariant distributions for the protons, identified either by ionization or by kinematical fitting to the final states $\mu^+p\pi^-$ and $\mu^+p\pi^-\pi^+\pi^-$, for Λ^0 and for K_S^0 are shown in Fig. 7 from the complete data sample. The proton and Λ^0 distributions are large in the backward hemisphere, but they also extend significantly into the region $X_F \geq 0$. Since the hadronic system has zero net change, one may guess that the proton multiplicity is about 0.5, so that the sample of 2567 events would include 1283 protons.[18] The number of protons identified and plotted in Fig. 7 is 628. The substantial number of protons not identified are thus analyzed as pions and represent a contamination in some of the distributions considered later. The significance of this contamination is, however, much reduced by the W cut at 4 GeV, which allows a wide enough rapidity range for current and target fragments to partially separate.[16]

We again show the invariant X_F distribution for positive hadrons in Fig. 8, but now separated into the two intervals of W specified on the figure. The complete range of Q^2 is used in the lower set of data, while the cut $1 \leq Q^2 < 45$ (GeV/c)^2 is used to remove the resonance-region events for the upper data set. There are no obvious differences between these distributions and, in both cases, the scaling or limiting fragmentation requirement of W independence is reasonably well satisfied. The same selections and comparisons are made for the negative hadrons in Fig. 9.

In order to study the behavior of the central

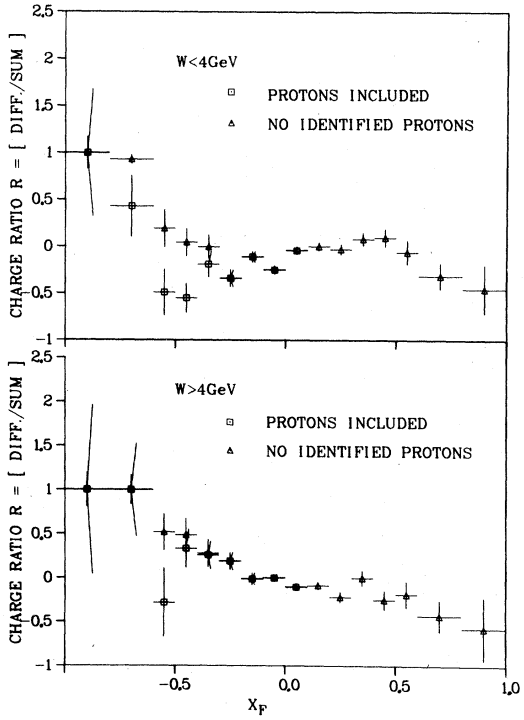

FIG. 12. The charge ratio R defined as $(h^+ - h^-)/(h^+ + h^-)$ as a function of X_F in $\bar{\nu}p \to \mu^+ h^\pm X$ events with the selections $W < 4$ GeV and $W \geq 4$ GeV. The charge ratio is shown in two sets of data, including and excluding the visually identified protons.

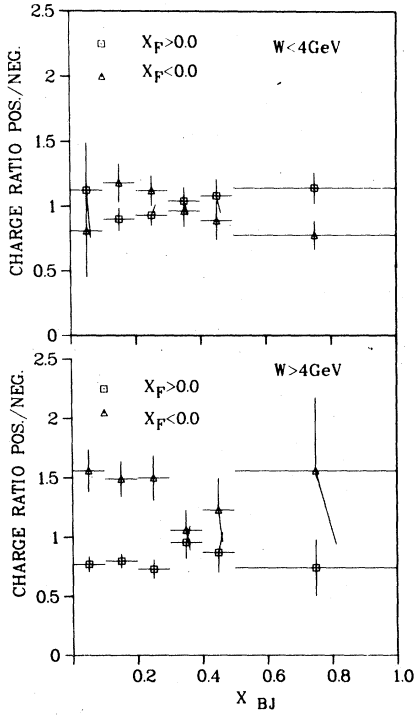

FIG. 13. The ratio of positive to negative hadrons for $\bar{\nu}p \to \mu^+ h^\pm X$ events with $W < 4.0$ GeV and $W \geq 4.0$ GeV as a function of X_{BJ}. The data are shown separately for $X_F < 0$ and $X_F \geq 0$.

region, we show the single-particle cross section $F(Y_R)$ for all charged particles as a function of rapidity Y_R, for three different intervals of W in Fig. 10. In the lowest W interval, $1 \leq W < 3$ GeV in Fig. 10(a), the proton contribution may be discerned as a shoulder below rapidity zero. A central plateau only develops for the highest W selection ($W \geq 5$ GeV) shown in Fig. 10(c).

In order to compare our rapidity distribution with that observed in pp interactions, we select equivalent c.m. energies using the available energy, defined as $(W - M_p)$ in $\bar{\nu}p$ interactions and $(\sqrt{s} - 2M_p)$ in pp interactions. In Fig. 11, we compare, for the same available energy, the distribution $(1/\sigma_{\text{inel}})d\sigma/dY_R$ for the reaction[19] $pp \to \pi^{\pm}X$ with that for our experiment. For the $\bar{\nu}p$ and pp data of Fig. 11, the available energies are 4.8 and 4.9 GeV, respectively. Protons recognized as such by ionization are removed from both samples of data. This procedure is somewhat less efficient for the $\bar{\nu}p$ case than for the pp experiment. However, we see from Fig. 11 that the plateau is much higher for $\bar{\nu}p$ than for pp, while the integral of the $\bar{\nu}p$ distribution is only 1.15 times that of the pp distribution. A small correction to the $\bar{\nu}p$ sample is needed for the missing one-prong events. Our estimate shows that after this correction, the charge multiplicites are equal in the two cases, but the plateau is still higher for the $\bar{\nu}p$ case than for the pp data. This difference may be connected with the fact that the neutrino data covers a range of c.m. energies, whereas the pp data is at a fixed c.m. energy.

We define the charge ratio to be $(h^+ - h^-)/(h^+ + h^-)$ and show its variation with X_F for two different W selections in Fig. 12. Although the invariant X_F distributions are asymmetric about zero, the net charge distribution is well centered on zero for the data with the higher W selection. The relativistic oscillator model of lepton-nucleon reactions suggested by Osborne would predict symmetric distributions in the invariant cross section for π^+ and for π^-.[20] Moreover, the π^- would exceed the π^+ in the backward hemisphere. This is not supported by the data of Fig. 12.

To see if the charge ratio, now taken to be positive divided by negative hadron number, shows the influence of the fragmenting quark, we plot

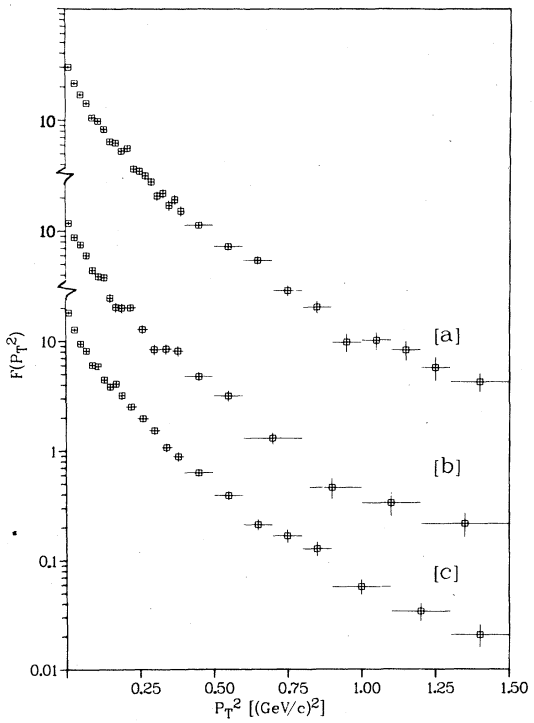

FIG. 14. The distribution in P_T^2 for charged hadrons in $\bar{\nu}p \to \mu^+ h^{\pm} X$ events for (a) all hadrons, (b) hadrons with $X_F < 0$, and (c) hadrons with $X_F \geq 0$. The ordinate scale applies to the data sample (c). The data points (b) for $X_F < 0$ are displaced upwards by a decade. The data points (a) for $X_F \geq 0$ are displaced upwards by two decades.

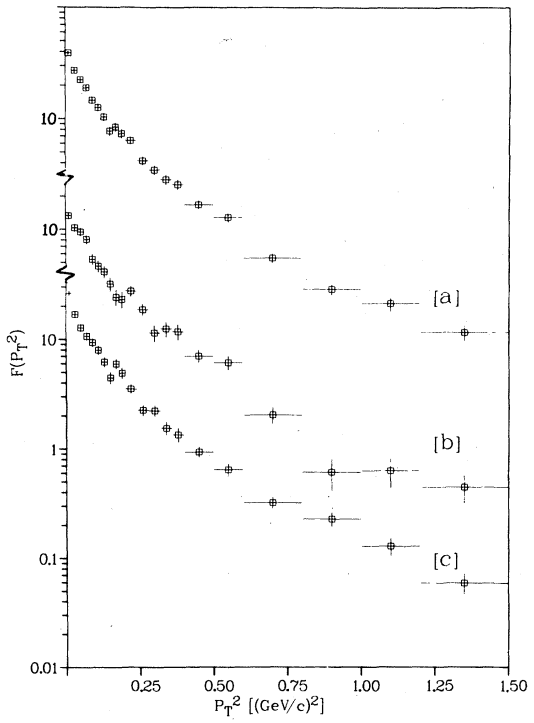

FIG. 15. The distribution in P_T^2 for charged hadrons in $\bar{\nu}p \to \mu^+ h^{\pm} X$ events with $W \geq 4$ GeV and $1 \leq Q^2 \leq 45$ (GeV/c)^2 for (a) all hadrons, (b) hadrons with $X_F < 0$, and (c) hadrons with $X_F \geq 0$. The ordinate scale applies to the data sample (c). The data points (b) for $X_F < 0$ are displaced upwards by a decade. The data points (a) for $X_F \geq 0$ are displaced upwards by two decades.

TABLE I. The distribution in P_T^2 fitted to the forms (a) $A[\exp(-BP_T^2)+C\exp(-DP_T^2)]$ and (b) $A\exp(-BP_T-CP_T^2)$. For (a) [(b)], the units of B and C below are $(\mathrm{GeV}/c)^{-2}$ [$(\mathrm{GeV}/c)^{-1}$] and dimensionless [$(\mathrm{GeV}/c)^{-2}$], respectively.

Fit	x_F	A [$(\mathrm{GeV}/c)^{-1}$]	B	C	D [$(\mathrm{GeV}/c)^{-2}$]	χ^2/NDF
			$W>1$ GeV $Q^2\leq 45$ $(\mathrm{GeV}/c)^2$			
(a)	All	22.9 ± 0.75	15.2 ± 1.5	0.38 ± 0.03	4.4 ± 0.15	$\frac{55}{26}$
(a)	≥0.0	13.9 ± 0.6	14.8 ± 2.9	0.34 ± 0.06	4.4 ± 0.35	$\frac{43}{19}$
(a)	<0.0	9.5 ± 0.6	15.9 ± 1.8	0.39 ± 0.11	4.6 ± 0.56	$\frac{31}{17}$
(b)	All	49.6 ± 0.6	4.5 ± 0.08	1.5 ± 0.15		$\frac{39}{27}$
(b)	≥0.0	29.3 ± 1.7	4.5 ± 0.3	1.7 ± 0.15		$\frac{20}{20}$
(b)	<0.0	19.0 ± 1.1	4.1 ± 0.15	2.1 ± 0.3		$\frac{33}{18}$
			$W>4$ GeV $1\leq Q^2\leq 45$ $(\mathrm{GeV}/c)^2$			
(a)	All	32.3 ± 2.1	13.1 ± 1.4	0.24 ± 0.08	3.5 ± 0.38	$\frac{29}{17}$
(a)	≥0.0	21.0 ± 2.1	11.5 ± 0.3	0.14 ± 0.05	2.9 ± 0.38	$\frac{30}{17}$
(a)	<0.0	11.9 ± 1.2	9.8 ± 1.1	0.14 ± 0.02	2.9 ± 0.15	$\frac{37}{17}$
(b)	All	66.9 ± 2.4	4.9 ± 0.15	0.8 ± 0.03		$\frac{20}{18}$
(b)	≥0.0	46.5 ± 4.2	5.6 ± 0.3	2.0 ± 0.3		$\frac{18}{18}$
(b)	<0.0	21.1 ± 2.9	3.8 ± 0.75	1.9 ± 0.9		$\frac{29}{18}$

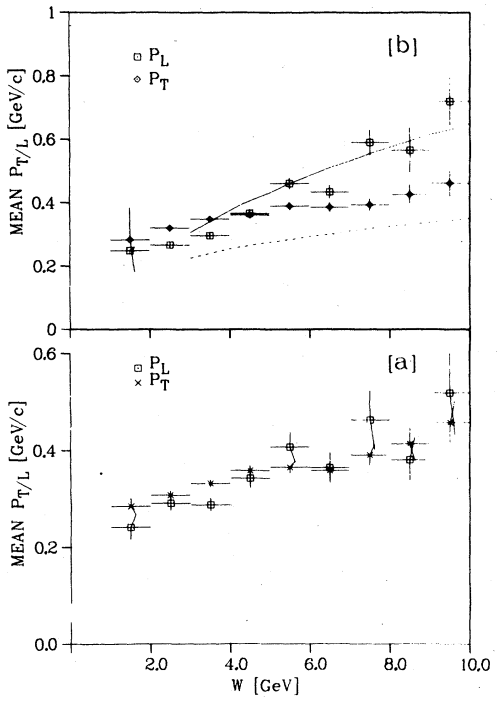

FIG. 16. The W dependence of mean P_T, $\langle P_T\rangle$, and mean P_L, $\langle P_L\rangle$, for $\bar{\nu}p\to\mu^+h^\pm X$ events for (a) $X_F<0$ and (b) $X_F\geq 0$. The data are given for the hadronic c.m. system. The lines on (b) show the results from e^+e^- annihilation at the same c.m. energy.

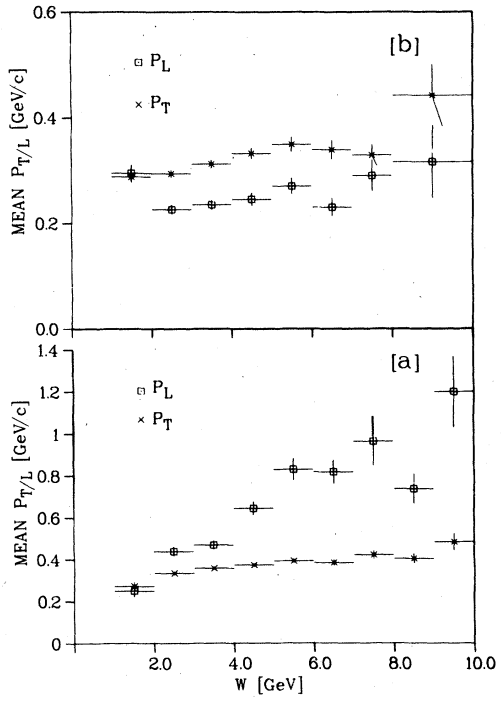

FIG. 17. The W dependence of mean P_T, $\langle P_T\rangle$, and mean P_L, $\langle P_L\rangle$, for $\bar{\nu}p\to\mu^+h^\pm X$ events for (a) $X_F<0$ and (b) $X_F\geq 0$. The data are given for the Breit frame.

this ratio as a function of X_{BJ} in Fig. 13. There is no sign of any change in the charge ratio for $X_{BJ} < 0.2$, where the sea quarks are known to contribute, for any of the data selections used in Fig. 13.

Before presenting the transverse-momentum properties of the events, some technical problems must be discussed. For neutrino reactions, momentum components normal to the lepton plane, P_T^{out}, are better determined than those in the plane since the latter reflect uncertainties in the Q direction introduced by uncertainties in the neutrino energy estimation. An alternative to selecting the hadron transverse momentum relative to the Q direction is to define it with respect to the vector momentum of the charged hadronic system. We find no significant differences between distributions in these two quantities, so we use P_T relative to the Q direction. These distributions also show the expected relationship to P_T^{out}.

In lepton production, it is well known that the distribution in P_T^2,

$$F(P_T^2) = \frac{1}{N_{ev}} \frac{dN_T}{dP_T^2}, \tag{12}$$

is not described by a simple Gaussian form.[2-4] This is clearly seen for all charged hadrons in the complete data sample shown as the upper set of data in Fig. 14. It is also true for charged hadrons with $X_F < 0$ and those with $X_F \geq 0.0$, in data samples 14(b) and 14(c), respectively. The distributions 14(b) and 14(a) have been displaced upwards by one and two decades, respectively. The corresponding distributions for events with $W \geq 4$ GeV and $1 \leq Q^2 < 45$ (GeV/c)^2 are shown in Fig. 15. These P_T^2 distributions have been fitted using two different functional forms with the results given in Table I. The best fit is obtained by fitting to $A\exp(-BP_T - CP_T^2)$. However, no striking difference appears between the results for the forward and backward systems in the hadronic c.m. system.

V. FRAGMENTATION OF THE d QUARK

The hadronic system resulting from deep-inelastic quark transitions should show the presence of jets of hadrons; jets resulting from both the single-quark parent and also possibly the diquark system may be expected. In a previous publication from this experiment,[21] the properties of $\bar{\nu}$-induced hadronic jets were studied in terms of

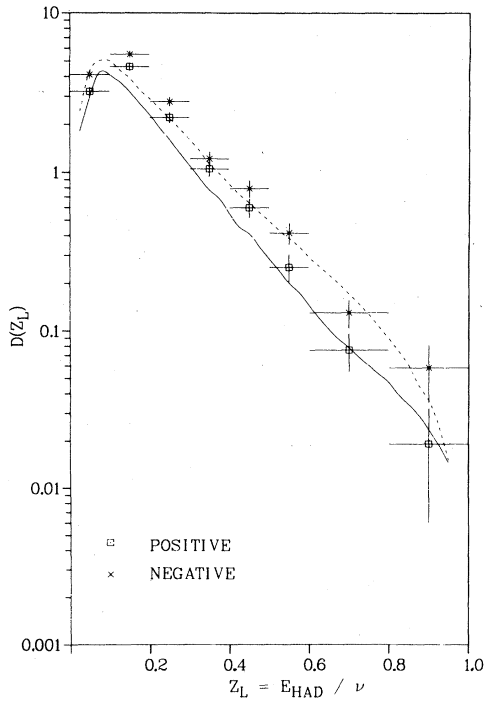

FIG. 18. The distribution in $Z_L = E_{HAD}/\nu$ for charged hadrons in $\bar{\nu}p \to \mu^+ h^\pm X$ events with $X_F \geq 0$, $W \geq 4$ GeV, and $1.0 \leq Q^2 < 45$ (GeV/c)^2. The positive and negative hadrons are shown separately. The curves show the results of the standard jet model, the solid line for positive hadrons, and the broken line for negative hadrons.

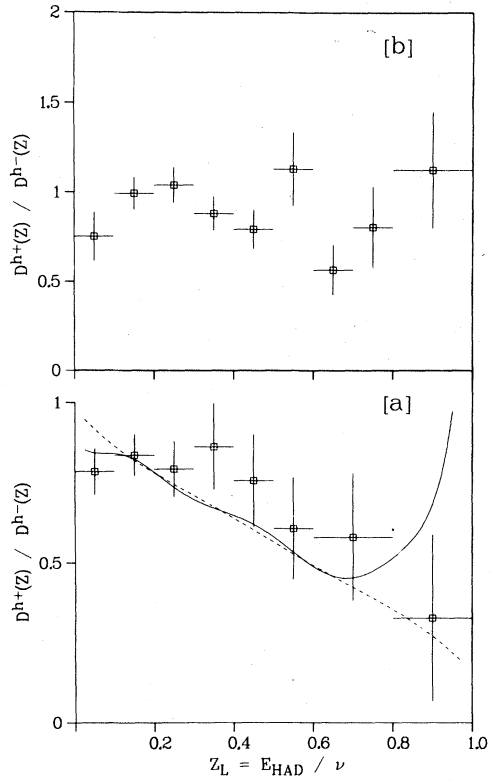

FIG. 19. The ratio of d-quark fragmentation functions $D_Z^h(Z)$ for positive and negative hadrons selected in $\bar{\nu}p \to \mu^+ h^\pm X$ events with $1.0 \leq Q^2 < 45$ (GeV/c)^2 for (a) $W \geq 4$ GeV and (b) $W < 4$ GeV.

sphericity, thrust, and energy flow. A description in terms of jets was seen to be reasonable only for the higher values of W, where the longitudinal momentum exceeded the transverse momentum. The general features were found to be in agreement with those observed for jets resulting from e^+e^- annihilation. This agreement is perhaps fortuitous since the current experiments are done at low energy. In neutrino interactions, the struck quark suffers a major acceleration and so may radiate gluons, whereas the spectator-diquark system is relatively unaffected by the primary hard collision. So some differences may be expected between the e^+e^- and the ν data.

The size of the jet in simplest terms may be described by the ratio of the average value of the transverse to the longitudinal momentum. The $\langle P_T \rangle$ and $\langle P_L \rangle$ are shown as a function of W for charged hadrons with $X_F < 0$ and those with $X_F \geq 0$ in Figs. 16(a) and 16(b), respectively. In Fig. 16(b), the lines show the corresponding results from e^+e^- annihilation,[22] the solid curve being for P_L and the dashed for P_T. In that case, the $\langle P_T \rangle$ is measured relative to the thrust axis which may explain the somewhat lower values observed in these data as compared to our neutrino experiment. The $\langle P_L \rangle$ only begins to exceed $\langle P_T \rangle$ for $W \gtrsim 4$ GeV, emphasizing again that the jet concept is only meaningful for large W.

It has been suggested that in first-order QCD, the jet associated with the spectator diquark should be narrower than the single-quark jet.[23] The $\langle P_T \rangle$ and $\langle P_L \rangle$ for the hadrons in the backward hemisphere of the hadronic c.m., shown in Fig. 16(a), suggest that at high W, the diquark jet is wider than the quark jet in this system. However, in Fig. 17, this comparison is made in the Breit frame and here the diquark jet is narrower. This is an example of how the low energy of the present experiments make the results of such studies difficult to interpret.

We now present further properties of the jets resulting from d-quark fragmentation and compare them to the "standard jet model" of Field and Feynman.[8] Comparison will also be made between the properties of the single-quark and the diquark jets.

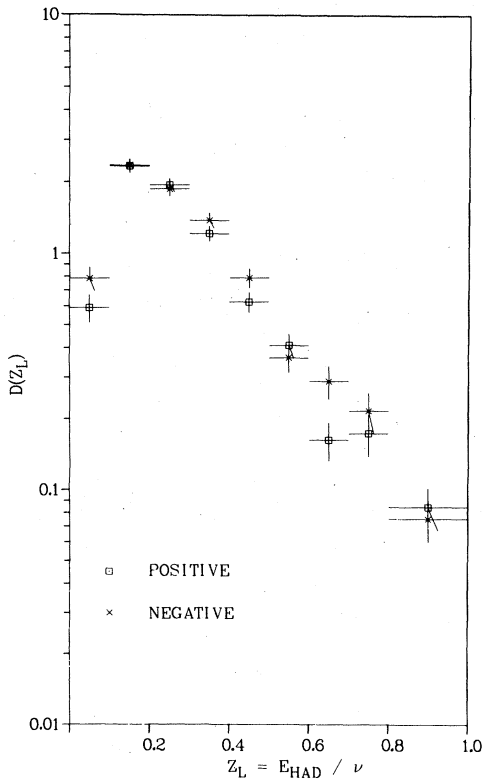

FIG. 20. The distribution in $Z_L = E_{\rm HAD}/\nu$ for positive and negative hadrons in $\bar{\nu}p \to \mu^+ h^\pm X$ events with $X_F > 0$, $W < 4$ GeV, and $1.0 \leq Q^2 < 45$ (GeV/c)^2.

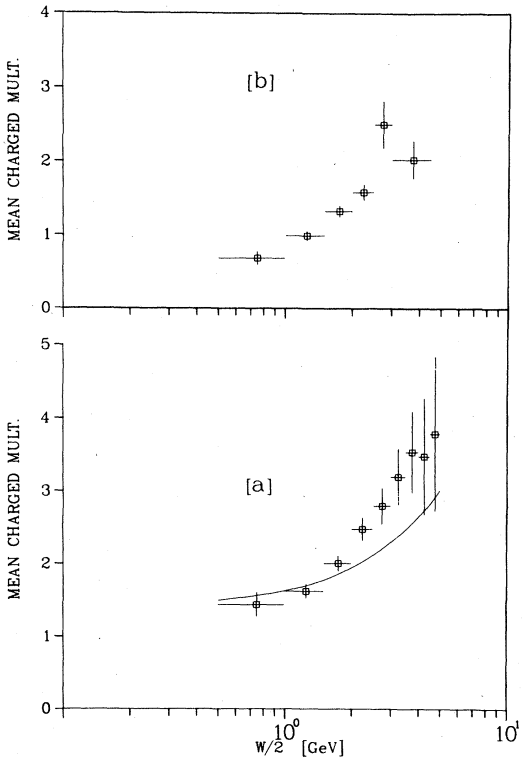

FIG. 21. The average charged-hadron multiplicity in $\bar{\nu}p \to \mu^+ h^\pm X$ events as a function of hadronic mass W for (a) $X_F \geq 0$ and (b) $X_F < 0$. The curve in (a) represents e^+e^- data selected as the charge multiplicity for one hemisphere at an energy of $\sqrt{s}/2$.

A. Fragmentation functions

The fragmentation function for a quark of type q to produce hadron-type h is defined to be

$$D_Z^h(Z) = \frac{1}{N_{ev}} \frac{dN_h}{dZ} , \tag{13}$$

i.e., the hadron density per unit of Z per event. The resolution in the energy-sharing variable Z is worst for high Z where $\delta Z/Z \approx 0.1$. The first moment of the fragmentation function is then the multiplicity of hadron h. The charge ratio h^+/h^- is just the ratio of the corresponding fragmentation functions.

In the simple QPM, the functions $D_q^h(z)$ are independent of the interaction producing the quark, so, as emphasized by Sehgal,[6] the same functions should apply in leptoproduction, e^+e^- annihilation, and high-P_T hadronic interactions, where it is claimed that quark jets have been observed. Moreover, the assumptions of charge-conjugation invariance and I-spin symmetry relate the different D_q^h functions so that the rates for charged-pion production, for example, in the above processes, should be related in a straightforward way.

With the selections $W > 4$ GeV/c, $1 \leq Q^2 < 45$ (GeV/c)^2 and $X_F \geq 0$, our fragmentation functions $D_q^{h^+}(Z)$ and $D_q^{h^-}(Z)$ are shown in Fig. 18. The lines show, for comparison, the predictions of the standard jet model generated according to the Q^2 and W distributions observed in this experiment. The agreement with our data is quite good for $Z_L \gtrsim 0.2$. We note in passing that data are usually compared to the prediction of the standard jet model calculated for 10-GeV quarks.[8]

In Fig. 19(a) we show the ratio of the fragmentation functions for positive and negative hadrons compared to the predictions of the standard model calculated for a 10-GeV quark (broken line) and for the kinematics appropriate to this experiment (full line). The differences between the two predictions at large Z are attributable to the consequences of resonance production and the large resonance Q values compared to the low jet energy. However, in all model comparisons of this kind, it is important to recognize that the constraints of charge and energy balance operate to produce similar effects.[3,4]

In Fig. 19(b), we show the corresponding dis-

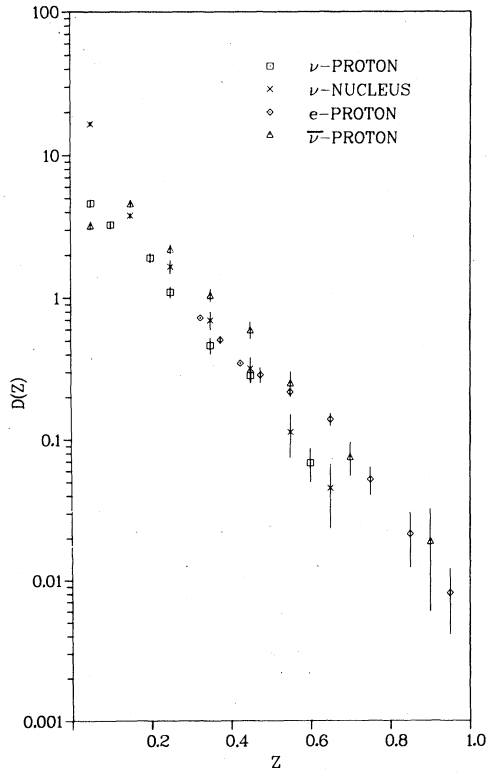

FIG. 22. The Z distribution for positive hadrons in $\overline{\nu}p \rightarrow \mu^+h^+X$ events compared to that for negative hadrons from νp (Ref. 4) and νN (Ref. 3) reactions and to π^- from ep interactions (Ref. 7).

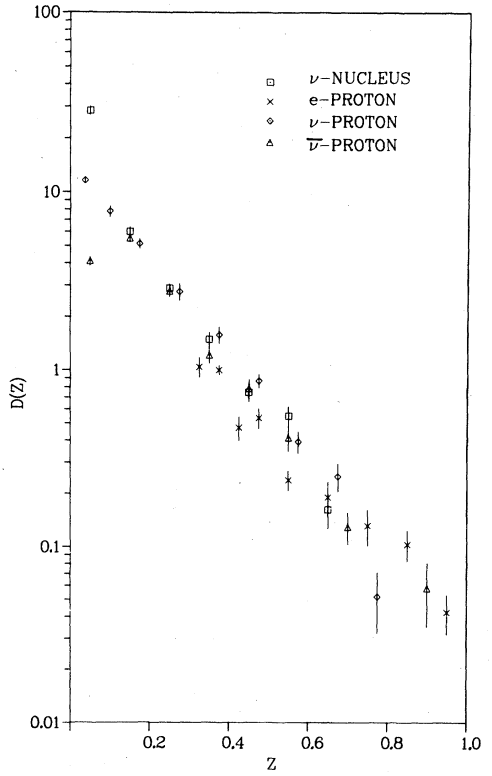

FIG. 23. The Z distribution for negative hadrons in $\overline{\nu}p \rightarrow \mu^+h^-X$ events compared to those for positive hadrons from νp (Ref. 4) and νN (Ref. 3) reactions, and to π^+ from ep interactions (Ref. 7).

tribution for events with $W<4$ GeV and $1 \leq Q^2 < 45$ $(\mathrm{GeV}/c)^2$. The charge asymmetry previously observed for the higher Z range in Fig. 19(a) is no longer apparent. Figure 20 shows the individual Z_L distributions for positive and negative hadrons with these same selections on W and Q^2.

The average charged-hadron multiplicity associated with the current jet, defined as hadrons with $X_F \geq 0.0$, is small as indicated in Fig. 21(a), where $\langle n_{ch} \rangle$ is shown versus $W/2$. At the low values of W encountered in present neutrino experiments, there is often only one charged hadron associated with the current jet. These data are compared to a parametrization of $\langle n_{ch} \rangle$ for one hemisphere at $\sqrt{s}/2$ in e^+e^- annihilation,[24] shown as the solid line. The neutrino data are in approximate agreement with the e^+e^- result but lie somewhat higher. The backward c.m. hemisphere data of Fig. 21(b) have somewhat lower values of $\langle n_{ch} \rangle$ consistent with the rapidity distributions of Fig. 10. However, these results depend strongly on whether the hadron c.m. or the Breit frame is used to define the jets.[16]

The Z_L distributions, shown in Fig. 18, may be compared to the corresponding distributions measured in $\nu p \to \mu^- hX$ and $ep \to e\pi^\pm X$ experiments. In both the νp and the $\bar{\nu} p$ data, no correction is made for the kaon contribution. However, since $\pi^\pm$ should dominate, agreement is expected between the $D(Z)$ measured for $\bar{\nu} p \to \mu^+ h^- X$, $\nu p \to \mu^- h^+ X$, and the electroproduction reaction[7] $ep \to e\pi^+ X$. Similar agreement is expected between $\bar{\nu} p \to \mu^+ h^+ X$, $\nu p \to \mu^- h^- X$, and $ep \to e\pi^- X$. These comparisons are made in Figs. 22 and 23, respectively. The factor of 2 agreement is quite good in view of the slightly different data selections and the different definitions of the Z variable employed. At low Z, one also sees differences attributable to target fragmentation in the complex nucleus as compared to that for hydrogen.

The total charged-hadron rate per event from $\bar{\nu} p$ and νp interactions, and the e^+-e^- annihilation rate for one hemisphere below charm threshold,[25] are compared in Fig. 24. The agreement with the e^+-e^- data is quite good except, perhaps, at the highest Z values.

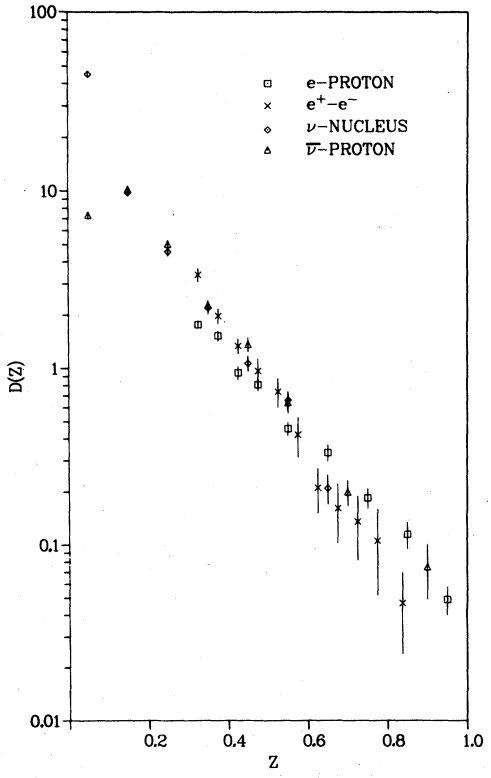

FIG. 24. The Z distribution for all charged hadrons from $\bar{\nu} p \to \mu^+ h^\pm X$ events compared to those for all charged hadrons from νN (Ref. 3), and ep (Ref. 7) reactions and to single hemisphere e^+e^- hadron production below charm threshold.

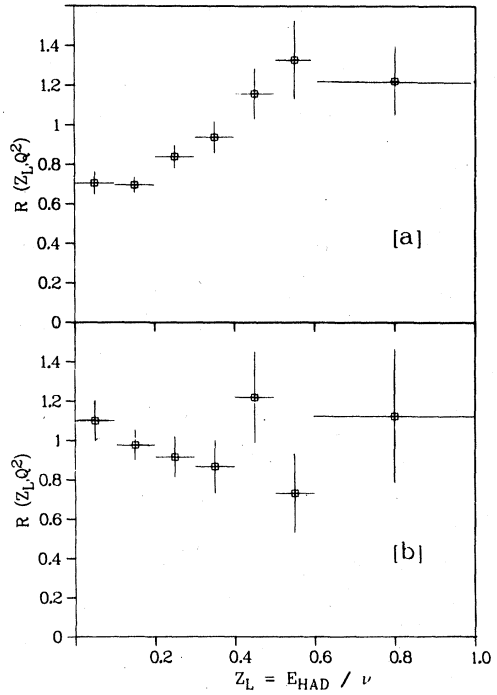

FIG. 25. The ratio of Z_L distributions for charged hadrons in $\bar{\nu} p \to \mu^+ h^\pm X$ events with $X_F \geq 0$ in the two Q^2 intervals; $1 \leq Q_1^2 < 4$ $(\mathrm{GeV}/c)^2$ and $4 \leq Q_2^2 < 45$ $(\mathrm{GeV}/c)^2$ for (a) $W \geq 1$ GeV and (b) $W \geq 4$ GeV.

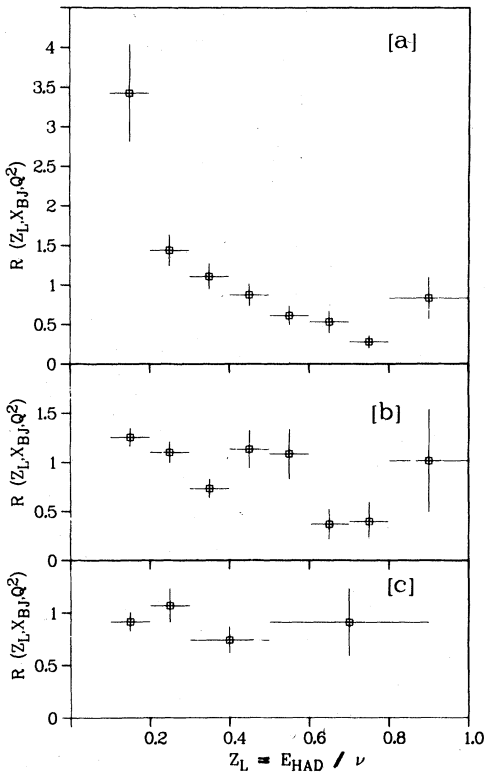

FIG. 26. The ratio of Z_L distributions for charged hadrons in $\bar{\nu}p \to \mu^+ h^\pm X$ events with $X_F \geq 0$ in the two X_{BJ} intervals, $X_{BJ} < 0.3$ and $0.3 \leq X_{BJ} < 1.0$ for (a) $W > 1$ GeV and $1 \leq Q^2 < 4$ (GeV/c)^2, (b) $W \geq 1$ GeV and $4 \leq Q^2 < 45$ (GeV/c)^2, and (c) $W \geq 4$ GeV, $4 \leq Q^2 < 45$ (GeV/c)^2.

B. Scaling, factorization, and higher-twist effects

Although the overall features of the data are well described by a simple quark-fragmentation model, at some level one may expect the D functions to exhibit scaling violations and lack of factorization, e.g., $D^h(Z, Q^2, X_{BJ})$. Such effects have been reported in νp interactions, although the effects appear to be confined to the low-W data.[26] The scaling deviations in the Z distribution of secondary hadrons were seen as a Q^2 dependence in the nonsinglet moments of the fragmentation function, consistent with the first-order QCD predictions. Our experiment does not show such behavior[16] and, in fact, for the same cuts as used in the νp experiment, the nonsinglet moments become negative in some regions of Q^2.

Rather than showing the nonsinglet moments, we choose to compare the shapes of the Z_L distributions, corrected for smearing, directly for different intervals of Q^2. We use $1 \leq Q_1^2 < 4$ (GeV/c)^2 and $4 \leq Q_2^2 < 45$ (GeV/c)^2 and compute the ratio of fragmentation functions

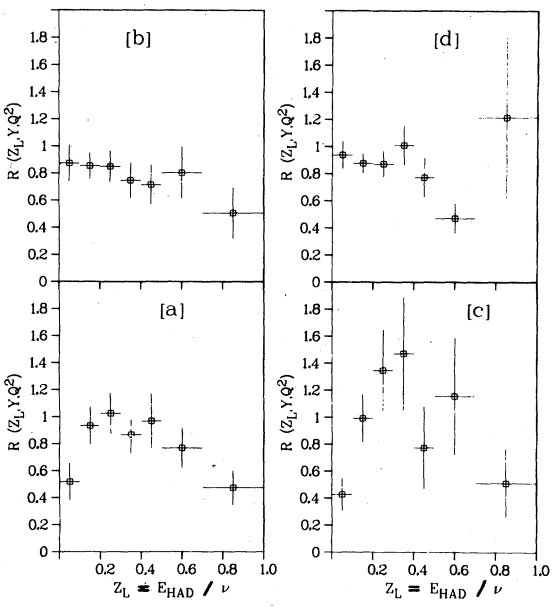

FIG. 27. The ratio of Z_L distributions for positive and negative hadrons in $\bar{\nu}p \to \mu^+ h^\pm X$ events with $X_F \geq 0$ in events with $W \geq 1$ GeV for (a) $Y < 0.3$ and $1 \leq Q^2 < 4$ (GeV/c)^2, (b) $Y \geq 0.3$ and $1 \leq Q^2 < 4$ (GeV/c)^2, (c) $Y < 0.3$ and $4 \leq Q^2 < 45$ (GeV/c)^2, and (d) $Y \geq 0.3$ and $4 \leq Q^2 < 45$ (GeV/c)^2 for positive and negative hadrons.

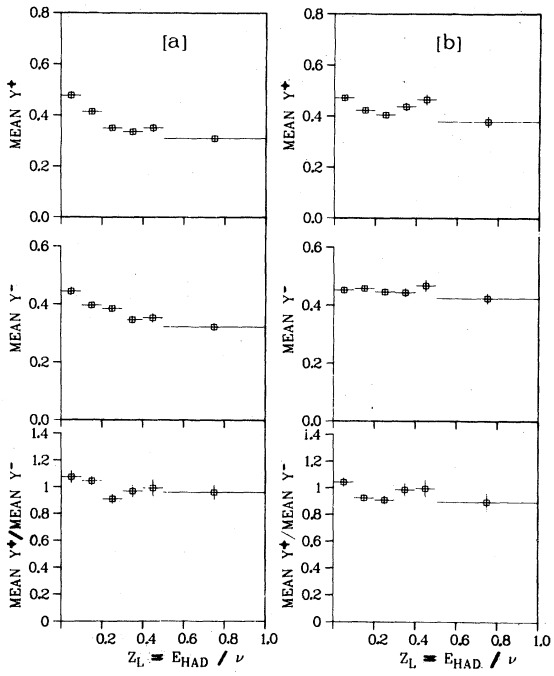

FIG. 28. The mean value of Y, shown as a function of Z_L for $\bar{\nu}p \to \mu^+ h^\pm X$ events with $W > 1$ GeV and $X_F > 0$ for (a) $1 \leq Q^2 < 5$ (GeV/c)^2 and (b) for $5 \leq Q^2 < 45$ (GeV/c)^2. The Z_L variation of the positive-to-negative hadrons is also shown.

$$R(Z_L,Q^2)=\frac{D^{h^\pm}(Z_L,Q_1^2)}{D^{h^\pm}(Z_L,Q_2^2)} \tag{14}$$

for hadrons with $X_F \geq 0$ excluding identified protons. Since we observe no significant difference between positive and negative hadrons, we combine them for this purpose.

The ratio is shown as a function of Z_L for the selections $W \geq 1$ GeV and $W \geq 4$ GeV in Figs. 25(a) and 25(b), respectively. There is no evidence in the latter data for any Q^2 dependence of the fragmentation for $W \geq 4$ GeV. The Q^2 dependence seen in Fig. 25(a) for $W \geq 1$ GeV, as pointed out in our previous publication,[16] is probably connected with the lack of separation of current and target fragments at these low W values.

We have shown,[16] using moments of the Z_L distribution, that factorization of the fragmentation function in terms of X_{BJ} is satisfied. One may also compare the shape of the fragmentation function for different intervals of X_{BJ},

$$R(Z_L,X_{BJ},Q^2)=\frac{D^{h^\pm}(Z_L,X_{BJ})}{D^{h^\pm}(Z_L,X'_{BJ})}. \tag{15}$$

Again, it is reasonable to combine positive and negative hadrons, and we use the selections X_{BJ} < 0.3 and $0.3 \leq X'_{BJ} < 1.0$. The ratio is shown as a function of Z_L for $W > 1$ GeV and both low- and high-Q^2 selections; $1 \leq Q^2 < 4$ (GeV/c)^2 and $4 \leq Q^2 < 45$ (GeV/c)^2 in Figs. 26(a) and 26(b), respectively. In Fig. 26(c), we show the ratio for events with $W \geq 4$ GeV and $4 \leq Q^2 < 45$ (GeV/c)^2. There is no compelling evidence for breakdown of the factorization hypothesis for $W > 4$ GeV. However, there is a clear falloff in the data of Fig. 26(a), which have low W and low Q^2.

We have also searched for a correlation between the variables Z_L and Y. Such a correlation would be expected as a result of higher-twist effects in the quark fragmentation. As pointed out by Berger,[27] the effects would appear at relatively low Q^2 and would add a $(1-Y)$ term to the cross section so the total Y dependence would be

$$\sigma(\bar{\nu}p \to \mu^+\pi^- X) \propto \left[D(Z)(1-Y)^2 + \frac{C}{Q^2}(1-Y)\right], \tag{16}$$

where C is a constant. Observation of such effects in νp interactions, where they may be more easily observable than in $\bar{\nu}p$ interactions, was recently reported.[28]

In order to look for any Z_L-Y correlation, we have directly compared the shape of the fragmentation function for different intervals of Y.

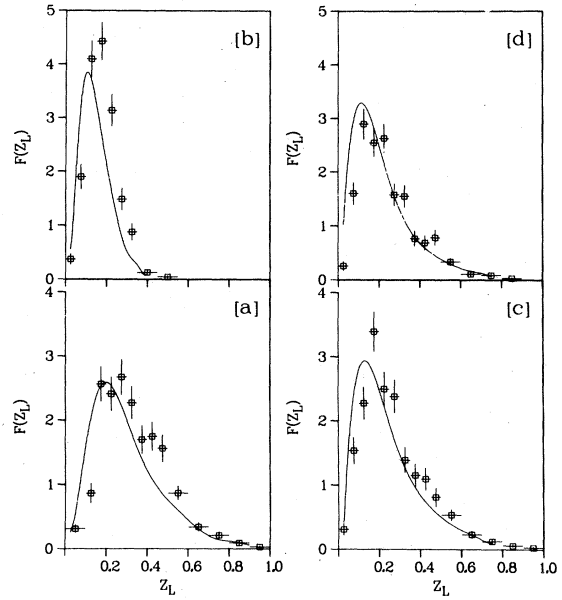

FIG. 29. The Z_L distribution for hadrons with $X_F \geq 0$ in $\bar{\nu}p \to \mu^+ h^\pm X$ events with $W \geq 4$ GeV and $1.0 \leq Q^2 < 45$ (GeV/c)^2 for (a) the highest-momentum charged hadron, (b) the second-highest-momentum charged hadron, (c) the highest-momentum negative hadron, and (d) the highest-momentum positive hadron. The curves are the predictions of the standard jet model.

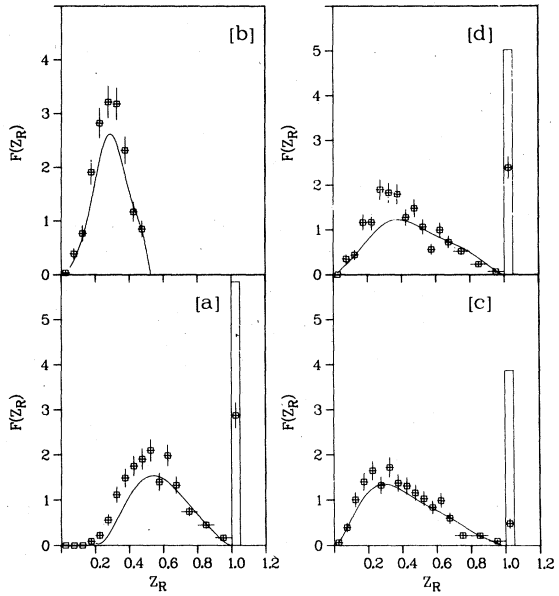

FIG. 30. The distribution $Z_R = Z_L^i / \sum Z_L^i$ for charged hadrons with $X_F > 0$ in $\bar{\nu}p \to \mu^+ h^\pm X$ events with $W \geq 4$ GeV and $Q^2 \geq 1$ (GeV/c)^2 for (a) the highest-momentum hadron, (b) the second-highest-momentum hadron, (c) the highest-momentum positive hadron, and (d) the highest-momentum negative hadron. The line represents the prediction of the standard jet model. The points above $Z_R = 1.0$ measure the relative frequency of jets with but a single charged particle.

The effect is expected to appear only for the leading charge, in this case the π^- from the d quark. The phase-space effects are divided out by comparing the π^- directly to the π^+:

$$R(Z_L, Y, Q^2) = \frac{D^{h^+}(Z_L, Y_1, Q^2)}{D^{h^-}(Z_L, Y_2, Q^2)} . \quad (17)$$

We use all events with $W \geq 1$ GeV and low Q^2, $1 \leq Q^2 < 4$ (GeV/c)^2, comparing the ratio for the subsamples with $0.1 \leq Y_1 < 0.3$ and $0.3 \leq Y_2 < 0.8$ in Figs. 27(a) and 27(b), respectively. The corresponding comparison for the high Q^2 range, $4 \leq Q^2 < 45$ (GeV/c)^2, is shown in Figs. 27(c) and 27(d). While in comparing Figs. 27(a) and 27(b), the dependence of the ratio on Z_L does differ between low- and high-Y selections, the same pattern is seen in comparing Figs. 27(c) and 27(d), i.e., we see no difference between the low and high Q^2 ranges.

We compare in Fig. 28 the mean value of Y for positive and negative hadrons as a function of Z_L using hadrons with $X_F \geq 0$ in events with $W \geq 1$ GeV. The ratio of positive to negative hadrons is also shown. In Fig. 28(a), the comparison is made for low Q^2, $1 \leq Q^2 < 5$ (GeV/c)^2. No difference is seen between distributions for the positive and negative hadrons. The same comparison is made for $5 \leq Q^2 < 45$ (GeV/c)^2 in Fig. 28(b). Again, no differences appear, and so our experiment shows no evidence for higher-twist effects. The νp reaction allows a more sensitive search for the higher-twist effects through a direct comparison of the shape of the Y distribution for different Z_L intervals.

C. Energy correlation

We define the d-quark jets by the event sample with $W > 4$ GeV and $1 \leq Q^2 < 45$ (GeV/c)^2, selecting only hadrons with $X_F \geq 0$. The distribution in Z_L for the charged hadrons with the highest and with the second highest momentum amongst the current-quark fragments are given in Figs. 29(a) and 29(b), respectively. It has been pointed out that the gross features of these distributions are well described by phase space.[3,4] However, reasonable agreement is also obtained with the standard jet model generated for the conditions of our experiment, as shown by the curves. The normalization difference, seen in Fig. 29(b) for the second-highest-momentum charged particle, is related to the higher fraction of single-charged-particle jets predicted by the model as compared to our data. Similarly, good agreement with the standard jet model is seen for the Z_L distributions

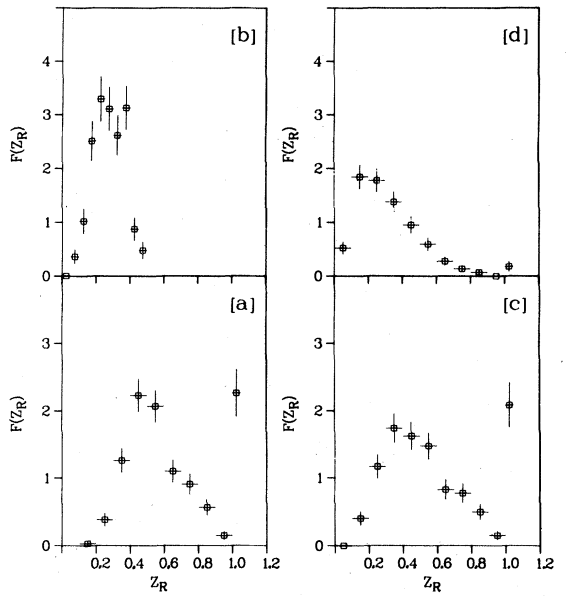

FIG. 31. The distribution in $Z_R = Z_L^i / \sum Z_L^i$ for charged hadrons with $X_F > 0$ in $\nu p \to \mu^- h^\pm X$ events with $W \geq 4$ GeV and $1 \leq Q^2 < 45$ (GeV/c)^2 for (a) the highest-momentum hadron, (b) the second-highest-momentum hadron, (c) the highest-momentum positive hadron, and (d) the highest-momentum negative hadron.

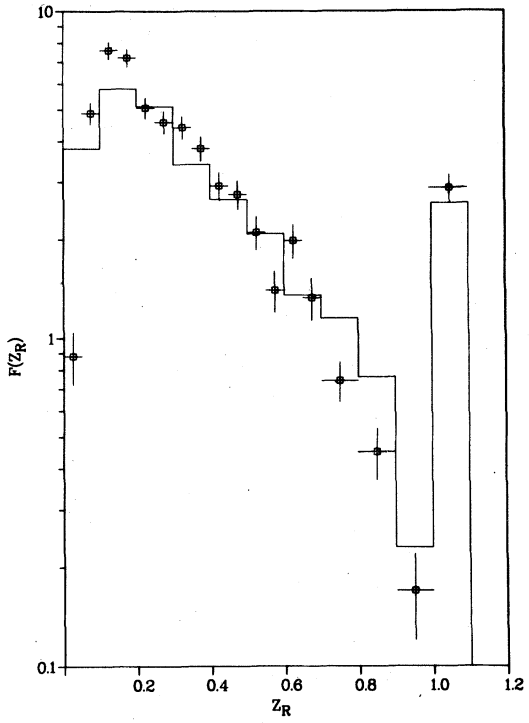

FIG. 32. Distribution in $Z_R = Z_L^i / \sum Z_L^i$ for all charged hadrons with $X_F > 0$ in $\bar{\nu} p \to \mu^+ h^\pm X$ events with $W \geq 4$ GeV and $1 \leq Q^2 < 45$ GeV^2. Shown for comparison in the histogram is a similar distribution measured in high-P_T hadron production in pp collisions at $\sqrt{s} = 53$ GeV.

of the highest-momentum negative and positive hadrons in the current-quark jet fragments, shown in Figs. 29(c) and 29(d), respectively.

As pointed out by Field and Feynman, these distributions may also be presented in terms of the variable $Z_R = Z_L^i / \sum Z_L^i$. The distributions given in Fig. 29 are plotted as a function of Z_R in Fig. 30. The peak at $Z_R = 1$ shows that it is quite common for these low-energy jets to contain only one charged particle. Our results show that the highest- and second-highest momentum charged hadrons carry, on average, $(34 \pm 2)\%$ and $(18 \pm 1)\%$ of the jet energy, respectively. Using the neutrino events resulting from the background neutrinos in the broad-band exposure of this experiment, we obtain similar data for the u-quark fragmentation, as shown in Fig. 31.

In Fig. 32, we compare the Z_R distribution for *all* charged hadrons in the current jet in $\bar{\nu}p$ interactions with the similar distribution for jets produced in high-P_T proton-proton collisions at $\sqrt{s} = 53$ GeV measured at the CERN Intersecting Storage Rings[29] and shown as the histogram. The agreement is quite striking.

D. Charge correlation

Field and Feynman have stressed the importance of studying charge properties to confirm that the jets actually arise from quarks. A comparison of our measured net-charge distribution with the prediction of the standard jet model is shown in Fig. 33; as a function of $\ln X_F$ in the hadron c.m. frame in Fig. 33(a) and as a function of $\ln Z_B$ in the Breit frame in Fig. 33(b). The agreement with the model, calculated for the kinematic conditions of our experiment, is reasonable in both cases. The dashed line shows, for comparison, the prediction from our Monte Carlo program to illustrate the phase-space restrictions. The Monte Carlo prediction is, of course, constrained by the way in which the protons are generated and the net charge is predicted to change little with W. The forward charge distribution for the u quark, made using the νp data, is shown in Fig. 34(a). Undoubtedly, the difficulty of the separation of current-quark and target fragments is less important for this test in νp than for the $\bar{\nu}p$ case.

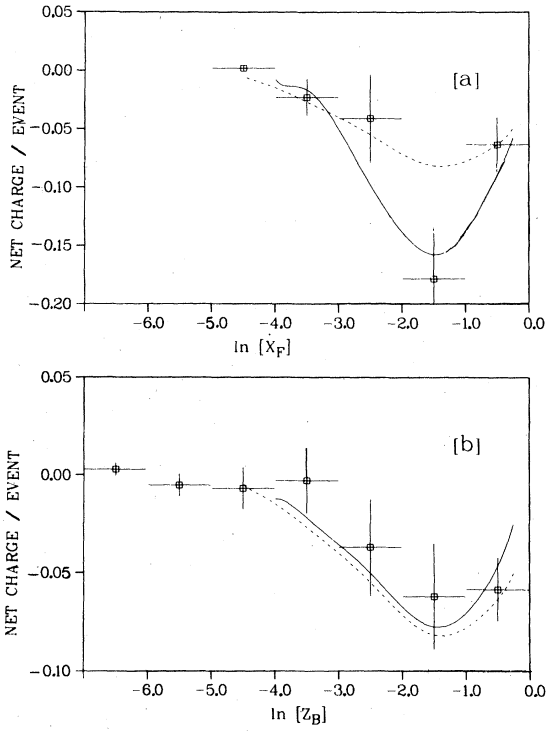

FIG. 33. Charge distribution for forward-going hadrons in $\bar{\nu}p \to \mu^+ h^\pm X$ events with $W \geq 4$ GeV and $1 \leq Q^2 < 45$ GeV^2 versus (a) $\ln X_F$ in the hadronic c.m. system where $X_F = 2P_L^*/W$ and (b) $\ln Z_B$ in the Breit frame, where $Z_B = 2P_L^B/Q$. The solid lines are from the standard jet model calculated for this experiment, and the dashed lines are the results of a phase-space calculation.

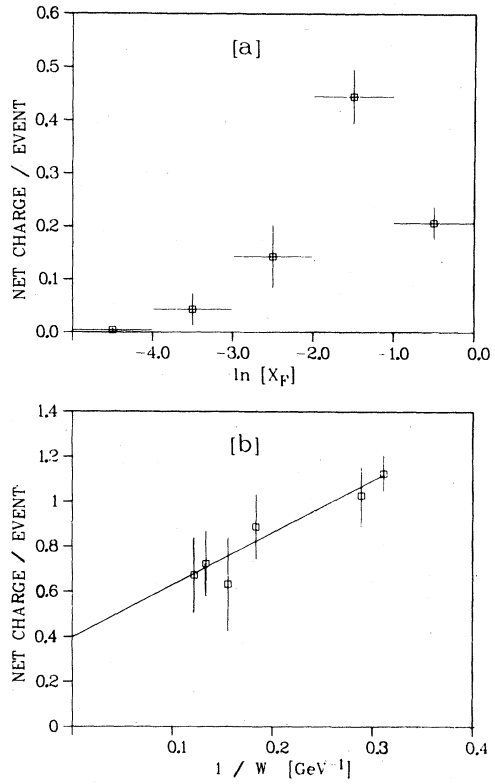

FIG. 34. (a) Charge distribution for forward-going hadrons in $\nu p \to \mu^- h^\pm X$ events with $W \geq 4$ GeV and $1 \leq Q^2 < 45$ (GeV/c)^2 versus $\ln X_F$ in the hadronic c.m. system where $x_F = 2P_L^*/W$, (b) the net forward charge in the hadron system for $\nu p \to \mu^- h^\pm X$ events as a function of W.

The problem of obtaining the true net forward charge in the high-energy limit of good separation between current and target fragments has been handled by extrapolating the net forward charge to high W versus $1/W$. A simple linear extrapolation is shown for our ν and $\bar{\nu}$ data in Figs. 34(b) and 35, respectively. The net forward charge extrapolated to $1/W=0$ is -0.25 ± 0.10 and -0.69 ± 0.16 for $\bar{\nu}p$ in the Breit frame and hadron frame, respectively. This frame dependence is not seen in a recent νp experiment that has better statistical precision than our experiment and where the net forward charge was observed to be frame independent.[5] Using our νp data, we find a forward charge of 0.4 ± 0.17 in the hadronic c.m. frame in agreement with the result of 0.55 ± 0.06 measured by the νp experiment at CERN.[5]

As previously discussed by Schmitz,[5] these experiments do not measure the quark charge itself, but rather the result of extracting u, d, or s quarks from the $q\bar{q}$ sea in the quark-dressing process.

E. Mean-P_T properties of quark fragments

In the naive QPM, the quarks have no transverse momentum within the struck hadron, and the fragments acquire a $P_T^{\rm frag}$ with respect to the struck quark from the hadronization process. The average transverse momentum $\langle P_T^2\rangle$ of the hadrons will then be independent of variables such as $X_{\rm BJ}$, Y, Q^2, W, etc., apart from trivial kinematic constraints and any instrumental effects.

However, in a perturbative QCD picture, the quark acquires an additional transverse component, $\langle P_T^2\rangle^{\rm QCD}$, as a result of gluon processes.[30] The quark itself may also have a primordial $\langle P_T^2\rangle^{\rm prim}$ inside the nucleon. The observed transverse momentum of the hadron will then result from folding the contributions from all these sources with appropriate weighting:

$$\langle P_T^2\rangle=[\langle P_T^2\rangle^{\rm QCD}+\langle P_T^2\rangle^{\rm prim}]Z^2+\langle P_T^2\rangle^{\rm frag}. \quad (18)$$

Dependencies of $\langle P_T^2\rangle$ on the variables $X_{\rm BJ}$, Y, Q^2, W, Z, etc., are introduced through the QCD term. In addition to the above dependence on Z, some calculations[31] suggest that the dependence of $\langle P_T^2\rangle^{\rm QCD}$ on Q^2 and W should vary like $W^2/\ln Q^2$. In these models, there should be a clear difference between the P_T dependence on the current-fragmentation region, particularly at high Z, and that of the target-fragmentation region where the QCD effects will be absent since the diquark system acts as a spectator.

We first look for a dependence of $\langle P_T\rangle$ on Q^2

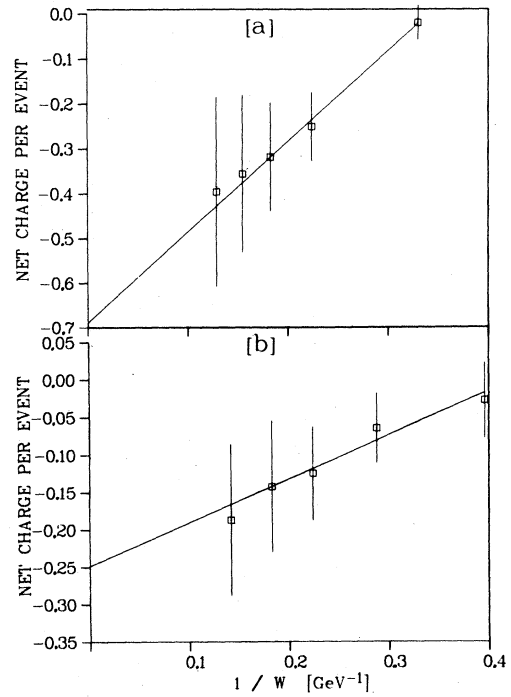

FIG. 35. The net forward charge as a function of W in $\bar{\nu}p\to\mu^+h^\pm X$ events in (a) the hadronic c.m. system and (b) in the Breit frame. The lines result from a least-squares fit to the data.

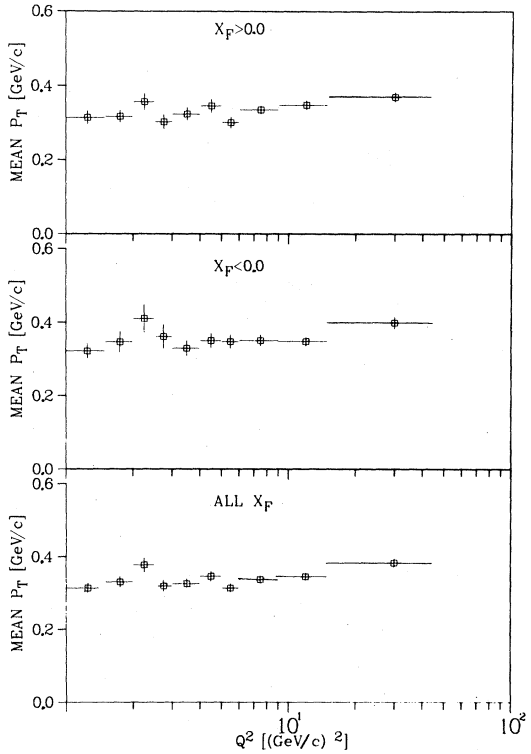

FIG. 36. The dependence of mean P_T, $\langle P_T\rangle$, on Q^2 for hadrons from $\bar{\nu}p\to\mu^+h^\pm X$ events with $W\geq4$ GeV for the selections $X_F<0$, $X_F\geq0$ and all X_F.

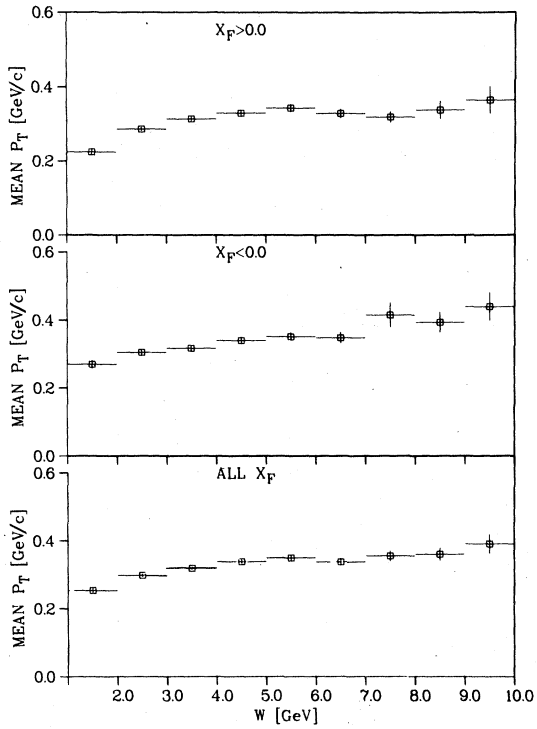

FIG. 37. The dependence of mean P_T, $\langle P_T \rangle$, on W for hadrons from $\bar{\nu}p \to \mu^+ h^\pm X$ events with $1.0 \leq Q^2 < 45$ (GeV/c)^2 for the selections $X_F \geq 0$, $X_F < 0$, and all X_F.

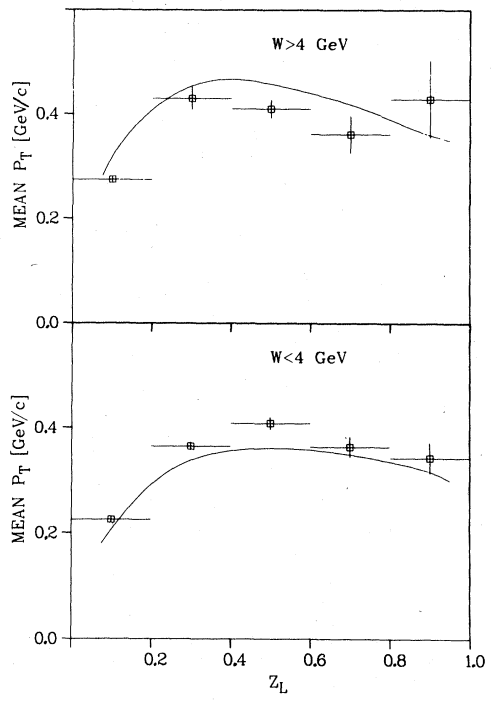

FIG. 39. The dependence of mean P_T, $\langle P_T \rangle$, on Z_L for hadrons from $\bar{\nu}p \to \mu^+ h^\pm X$ events with $1 \leq Q^2 < 45$ GeV^2 for $W \geq 4$ GeV and $W < 4$ GeV.

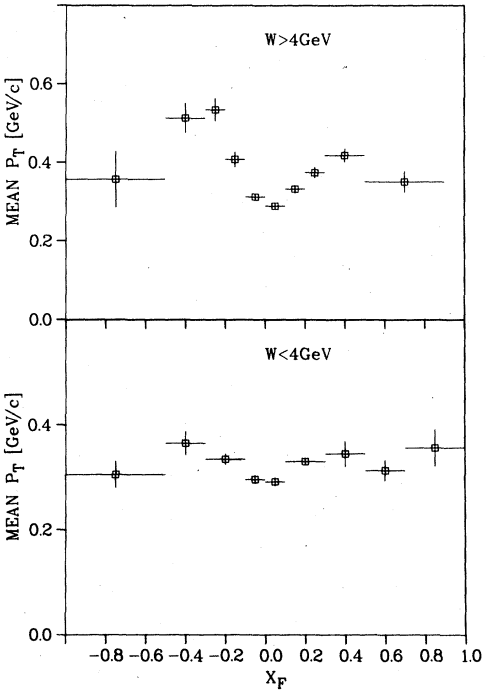

FIG. 38. The dependence of mean P_T, $\langle P_T \rangle$, on X_F for hadrons from $\bar{\nu}p \to \mu^+ h^\pm X$ events with $1 \leq Q^2 < 45$ (GeV/c)^2 for $W \geq 4$ GeV and $W < 4$ GeV.

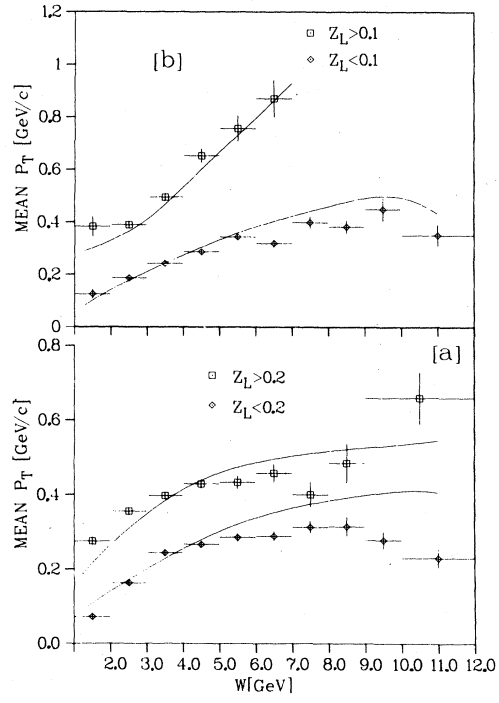

FIG. 40. The dependence of mean P_T, $\langle P_T \rangle$, on W for hadrons from $\bar{\nu}p \to \mu^+ h^\pm X$ events with $1.0 \leq Q^2 < 45$ (GeV/c)^2 for (a) $X_F \geq 0$ and (b) $X_F < 0$. The separation into two Z_L ranges is also shown. The lines show the predictions of a phase-space model.

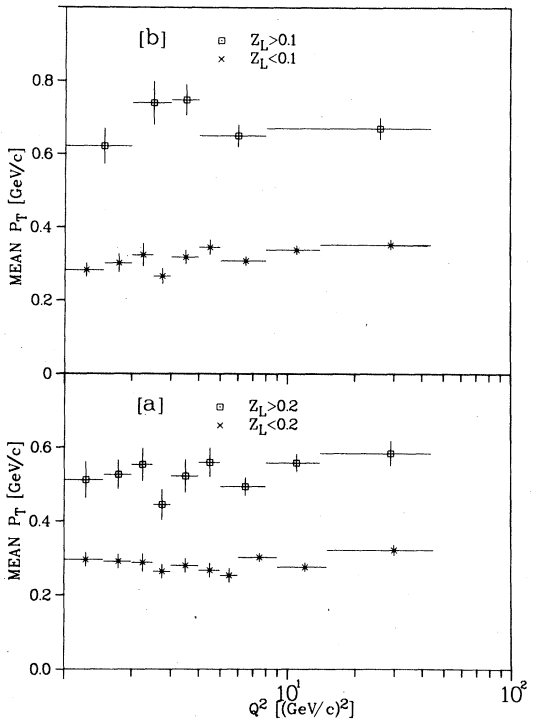

FIG. 41. The dependence of mean P_T, $\langle P_T \rangle$, on Q^2 for hadrons from $\bar{\nu}p \to \mu^+ h^\pm X$ events with $W \geq 4$ GeV for (a) $X_F \geq 0$ and (b) $X_F < 0$. The separation into two Z_L ranges is also shown.

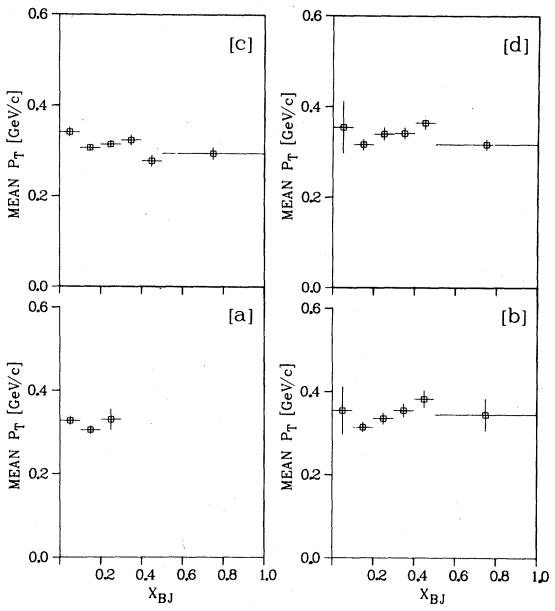

FIG. 43. The dependence of mean P_T, $\langle P_T \rangle$, on X_{BJ} for hadrons from $\bar{\nu}p \to \mu^+ h^\pm X$ events for (a) $W \geq 4$ GeV and $1 \leq Q^2 < 6$ (GeV/c)^2, (b) $W \geq 4$ GeV and $Q^2 \geq 6$ (GeV/c)^2, (c) $W \geq 1$ GeV and $1 \leq Q^2 < 6$ (GeV/c)^2, and (d) $W \geq 1$ GeV and $Q^2 \geq 6$ (GeV/c)^2.

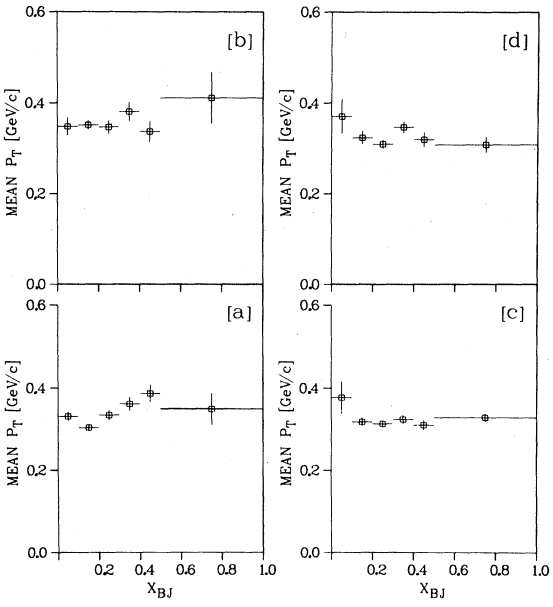

FIG. 42. The dependence of mean P_T, $\langle P_T \rangle$, on X_{BJ} for hadrons from $\bar{\nu}p \to \mu^+ h^\pm X$ events with $1 \leq Q^2 < 45$ (GeV/c)^2 for (a) $W \geq 4$ GeV, $X_F \geq 0$, (b) $W \geq 4$ GeV, $X_F < 0$, (c) $W < 4$ GeV, $X_F \geq 0$, and (d) $W < 4$ GeV, $X_F < 0$.

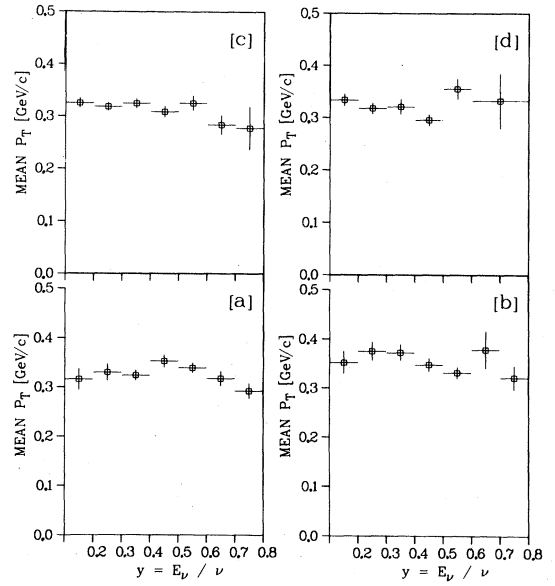

FIG. 44. The dependence of mean P_T, $\langle P_T \rangle$, on y for hadrons from $\bar{\nu}p \to \mu^+ h^\pm X$ events with $1 \leq Q^2 < 45$ (GeV/c)^2 for (a) $W \geq 4$ GeV and $X_F > 0$, (b) $W \geq 4$ GeV and $X_F < 0$, (c) $W < 4$ GeV and $X_F \geq 0$, (d) $W < 4$ GeV and $X_F < 0$.

and use the data with $W \geq 4$ GeV. In Fig. 36, we show $\langle P_T \rangle$ versus Q^2 for all charged hadrons and also for those with $X_F \geq 0$ and $X_F < 0$ separately. Little or no dependence on Q^2 is observed in these distributions. However, a weak but significant dependence of $\langle P_T \rangle$ on W is seen in the similar data of Fig. 37. The latter effect is similar to the slow $\langle P_T \rangle$ dependence on $\sqrt{s}$ seen in hadron physics, and it implies that any check for Q^2 dependence of $\langle P_T \rangle$ should be done at fixed W. Our data show no $\langle P_T \rangle$ variation with Q^2 in different W intervals.

As is well known, $\langle P_T \rangle$ increases with increasing X_F ($X_F \approx Z$ at high X_F) with a shape called the seagull effect.[2,3,32,33] This is a kinematical effect familiar from hadron physics, which stems from the lack of factorization of the inclusive cross section into X_F and $P_T{}^2$. Our data of Fig. 38 show that the seagull effect becomes more pronounced as W increases. This behavior is also reflected into other distributions as discussed below.

The explicit dependence of $\langle P_T \rangle$ on Z_L for the hadrons with $X_F \geq 0$ in events with $1 \leq Q^2 < 45$ (GeV/c)^2 is shown for $W < 4$ GeV and $W \geq 4$ GeV in the lower and upper parts of Fig. 39, respectively. The variation is accounted for by the phase-space prediction shown as the solid line. The variation of $\langle P_T \rangle$ with W is much more extreme than for the total sample shown in Fig. 37 if the high-Z hadrons are selected. This is seen in both the forward and backward hemispheres of the hadronic c.m. system in Figs. 40(a) and 40(b), respectively. However, the trend is again quite well described by the phase-space prediction as illustrated by the lines in Fig. 40. In Fig. 41, the corresponding plot is given for $\langle P_T \rangle$ as a function of Q^2. All of the $\langle P_T \rangle$ dependencies are well understood in terms of the seagull effect and phase-space requirements.

The question of factorization in the P_T dependence of the fragmentation process has been

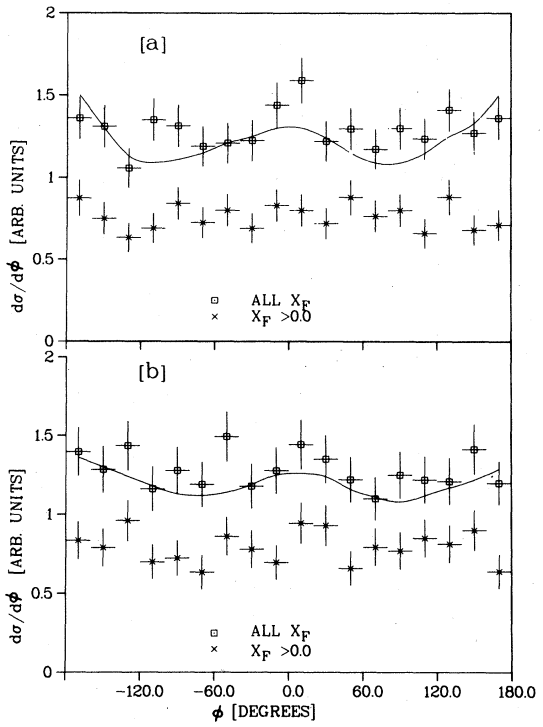

FIG. 45. The distribution in the azimuthal angle ϕ (defined in the text) for hadrons with the X_F selections indicated from $\bar{\nu}p \to \mu^+ h^\pm X$ events with $W \geq 4$ GeV; (a) $1 \leq Q^2 < 5$ (GeV/c)^2, (b) $5 \leq Q^2 < 45$ (GeV/c)^2. The curves are from a Monte Carlo calculation and show the expected instrumental bias.

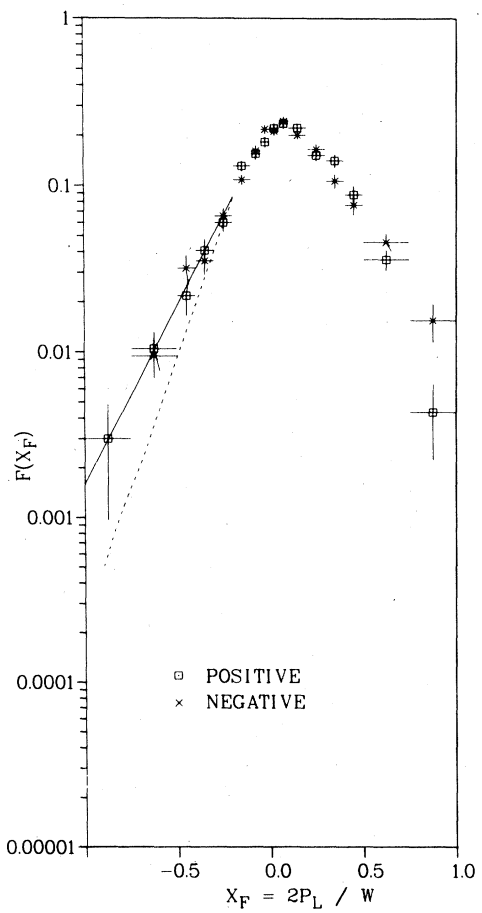

FIG. 46. The invariant distribution for positive hadrons (with identified protons removed) and for negative hadrons from $\bar{\nu}p \to \mu^+ h^\pm X$ events with $X_{BJ} \geq 0.2$. The lines show the corresponding distributions from the reaction $pp \to \pi^\pm X$ at 200 GeV. The π^+ data (solid line) are scaled by 0.75 and the π^- data (dashed line) by 1.5 in order to compare the leptonic and hadronic data to the model predictions.

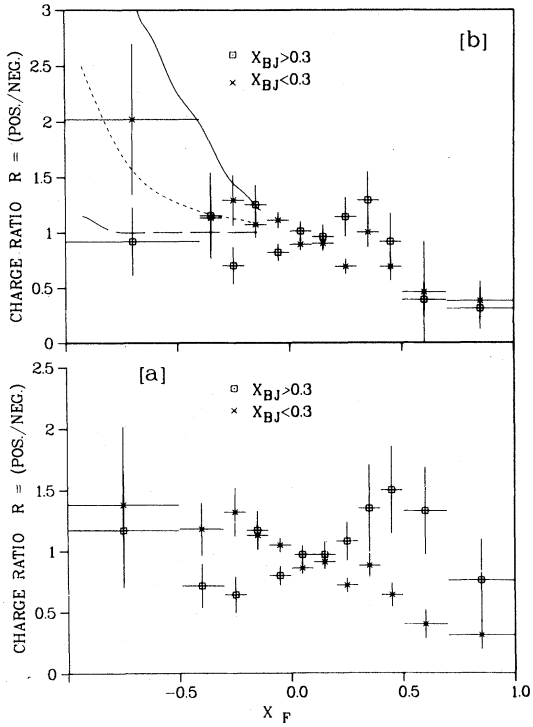

FIG. 47. The charge ratio of positive hadrons (with identified protons removed) to negative hadrons as a function of X_F for $\bar{\nu}p \to \mu^+ h^\pm X$ events with (a) $W>1$ GeV and $Q^2<45$ (GeV/c)^2, (b) $W>2$ GeV and $1 \leq Q^2 < 45$ (GeV/c)^2. The separation into two X_{BJ} selections is also shown. The solid line shows the corresponding distributions from the reactions $pp \to \pi^\pm X$ at 100–200 GeV. The other curves are theoretical predictions for the charge ratio at $X_{BJ}=0.1$ (dashed line) and $X_{BJ}=0.3$ (dot-dashed line).

studied for νp interactions, using nonsinglet moments of the P_T distribution.[5] The results show nonfactorization in X_{BJ} and P_T at fixed Q^2. To study this dependence, we use the complete Q^2 range, $1 \leq Q^2 < 45$ (GeV/c)^2, and compare the forward and backward hemispheres of the hadronic c.m. system at low and at high W. Figures 42(a) and 42(b) show $\langle P_T \rangle$ versus X_{BJ} for

TABLE II. Invariant x_F distribution fitted to the function $(2E^*/W)\,(1/N_{ev})\,dN/dx_F = A(1-|x_F|)^n$.

x_{bj} cut	x_F	Charge	n
None	≤ -0.05	+	2.9 ± 0.3
None	≥ 0.05	+	2.5 ± 0.2
None	≤ -0.05	−	2.8 ± 0.3
None	≥ 0.05	−	1.9 ± 0.2
≥ 0.2	≤ -0.05	+	3.0 ± 0.3
≥ 0.2	≥ 0.05	+	2.0 ± 0.2
≥ 0.2	≤ -0.05	−	3.3 ± 0.5
≥ 0.2	≥ 0.05	−	1.6 ± 0.2

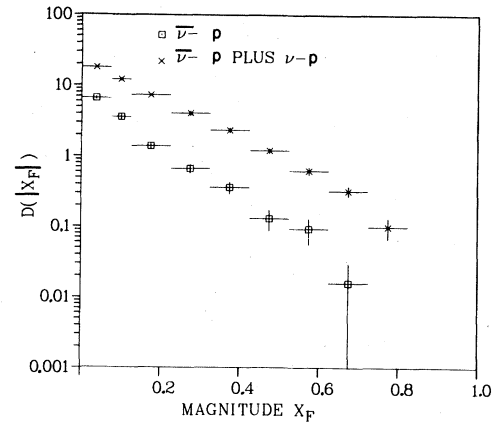

FIG. 48. The diquark (ud) fragmentation function for positive mesons $D(|X_F|) = (1/N_{ev})dN^{h^+}/d|X_F|$ for $X_F<0$ from the reaction $\bar{\nu}p \to \mu^+ h^+ X$ events with $W>4$ GeV and $1 \leq Q^2 < 45$ (GeV/c)^2. The upper set of data is the sum of the u- and d-quark fragmentation functions for the same ranges of W and Q^2 but selected with $X_F>0$ from $\nu p \to \mu^- h^+ X$ and $\bar{\nu}p \to \mu^+ h^+ X$ events, respectively.

$X_F \geq 0.0$ and $X_F < 0.0$, respectively, at $W \geq 4$ GeV. In neither case is there any significant dependence on X_{BJ}. The same conclusion holds for $W<4$ GeV as shown by Figs. 42(c) and 42(d). Overall, $\langle P_T \rangle$ does not depend significantly on X_{BJ} at fixed W.

We have also looked at the dependence of $\langle P_T \rangle$ on X_{BJ} at fixed Q^2. In Figs. 43(a) and 43(b) we show $\langle P_T \rangle$ as a function of X_{BJ} with the selections $1 \leq Q^2 < 6$ (GeV/c)^2 and $6 \leq Q^2 < 45$ (GeV/c)^2, respectively. Events with $W>1$ GeV are used, and we only show the data with $X_F \geq 0$. Again, there

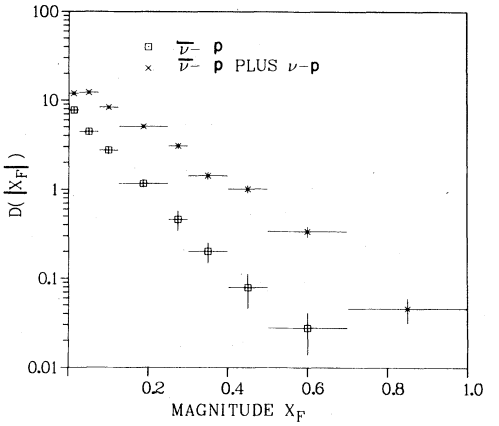

FIG. 49. The diquark (ud) fragmentation function for negative mesons $D(|X_F|) = (1/N_{ev})/dN^{h^-}/d|X_F|$ for $X_F<0$ from the reaction $\bar{\nu}p \to \mu^+ h^- X$ for $W \geq 4$ GeV and $1 \leq Q^2 < 45$ (GeV/c)^2. The upper set of data is the sum of the u- and d-quark fragmentation functions for the same ranges of W and Q^2 but selected with $X_F>0$ from $\nu p \to \mu^- h^- X$ and $\bar{\nu}p \to \mu^+ h^- X$ events, respectively.

is no obvious variation of $\langle P_T \rangle$ with X_{BJ}. In Figs. 43(c) and 43(d), we repeat the test for $W \geq 4$ GeV, where the selection criteria now limit the available range of X_{BJ}. We conclude that our data show no significant variation of $\langle P_T \rangle$ with X_{BJ} at either fixed W or fixed Q^2. Furthermore, there is no dependence of P_T on the scaling variable Y, for either current or target fragments or for high or low W, as seen in Fig. 44.

Somewhat related to these transverse properties are the azimuthal dependencies of the hadrons.[34,35] The coordinate frame used to study this employs the $\hat{z}$ axis along the Q^2 direction and y axis normal to the lepton plane, $\hat{y} = \hat{\nu} \times \hat{\mu}$. Then ϕ is measured from $\hat{x}$ to $\hat{y}$. For this study, events with $W \geq 4$ GeV are selected, the data are not corrected, and the small ϕ variations seen in Fig. 45 are consistent with the instrumentation effects expected and as demonstrated by the Monte Carlo simulation shown as the curve in Fig. 45. In Fig. 45(a), we select events with $1 \leq Q^2 \leq 5$ $(\mathrm{GeV}/c)^2$ and in Fig. 45(b), events with $5 \leq Q^2 \leq 45$ $(\mathrm{GeV}/c)^2$.

We conclude then that our experiment shows no significant differences from the expectations of the simple QPM. In order to see such effects in neutrino interactions, either higher-statistics data or data for higher values of W and Q^2 are required. Recent results[36,37] from neutrino interactions have shown an increase in $\langle P_T^2 \rangle$ with W for $W > 10$ GeV for the forward as compared to the backward jet. The data from these experiments agree with our results for $W < 10$ GeV.

VI. TARGET FRAGMENTATION

Attempts have been made to relate particle production in the target-fragmentation region for reactions initiated by pointlike probes to those for hadron-induced reactions at low transverse momentum. A specific prediction is that $\pi^+/\pi^- \approx 1$ in the proton-fragmentation region in $\bar{\nu}p \to \mu^+ \pi X$, whereas $\pi^+/\pi^- > 1$ for $\nu p \to \mu^- \pi X$.[38,39] Here the proton-fragmentation region is defined as $X_F \lesssim -0.5$ and large X_{BJ} is selected in order to ensure that the W boson removes a valence quark leaving a diquark system to fragment. In Fig. 46, we

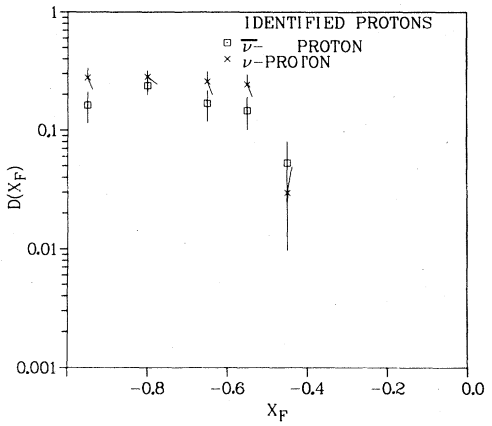

FIG. 50. The Feynman-X distribution for identified protons $D(X_F) = (1/N_{ev}) dN^p/dX_F$ in $\nu p \to \mu^- p X$ and $\bar{\nu}p \to \mu^+ p X$ events with $W \geq 4$ GeV.

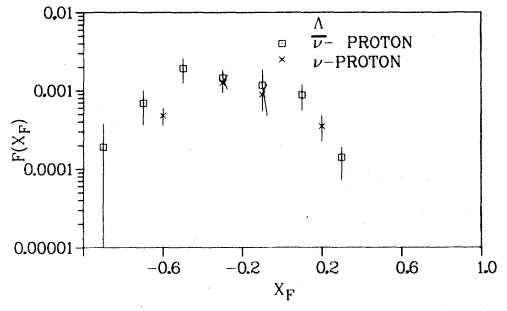

FIG. 51. The invariant cross section $F(X_F)$ for inclusive Λ^0 production in $\nu p \to \mu^- \Lambda^0 X$ and $\bar{\nu}p \to \mu^+ \Lambda^0 X$ events as a function of X_F.

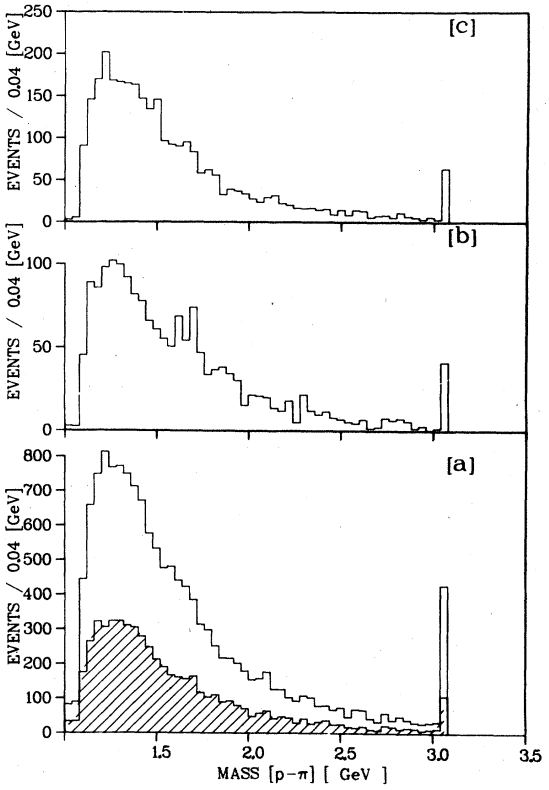

FIG. 52. The proton-pion effective mass in $\bar{\nu}p \to \mu^+ p \pi X$ events for (a) all combinations. Events with $X_{BJ} \geq 0.2$ are shown hatched; (b) $\pi^+ p$ combinations with $X_F < 0$, and (c) all $\pi^- p$ combinations with $X_F < 0$. Events with effective mass >3 GeV are shown in an overflow bin.

show the single-particle-invariant distributions for positive and negative hadrons from events with $X_{BJ} \geq 0.2$. The identified protons have been excluded so that for the region $X_F \lesssim -0.5$, we are comparing π^+ to π^-. The rates are seen to be very similar although the statistics near $X_F = -1.0$ preclude any firm conclusion.

Pion production in the proton-fragmentation region for hadron-induced breakup can be related to that using neutrinos.[39] It is suggested that $(1/\sigma_{inel})\, d\sigma/dX_F$ for $p \to \pi^+$ in hadronic processes should be equal to $\frac{4}{3}(1/\sigma_T)(d\sigma/dX_F)(\bar{\nu}p \to \mu^+\pi^+X)$. Similarly, $(1/\sigma_{inel})d\sigma/dX_F$ for $p \to \pi^-$ in the hadronic process should equal $\frac{2}{3}(1/\sigma_T)(d\sigma/dX_F)$ $(\bar{\nu}p \to \mu^+\pi^+X)$. In Fig. 46, we compare our results to data on pion production in proton-proton interactions.[40] The π^+ rate is multiplied by 0.75 and shown as the solid line, while the π^- rate is multiplied by 1.5 and appears as the broken line. The prediction is satisfied quite well for π^+ but less well for π^-.

The pion charge ratio in the target-fragmentation region, X_F close to -1.0, has been conjectured to depend strongly on X_{BJ}, since at low X_{BJ}, the W^- probe primarily removes sea partons from the proton leaving a (uud) fast core, whereas at high X_{BJ}, a u quark is selectively removed leaving a $(ud+\text{sea})$ core. The suggestion is that fast pions in the target-fragmentation region are then made by the fusion of a valence u (d) quark with a sea $\bar{d}$ ($\bar{u}$) quark for a π^+ (π^-).

At large X_F in the target-fragmentation region, the π^+/π^- ratio for low X_{BJ} should be large, falling to unity at high X_{BJ}.[38] The charge ratio, after removing all identified protons, is shown for the complete sample with the X_{BJ} selection indicated in Fig. 47(a). While the ratio is larger for small X_{BJ} than for large X_{BJ}, the difference is small. However, the region of interest at large $|X_F|$ is statistically limited. Because there may be complications associated with the resonance production, we also show the isotopic ratio for $W \geq 2$ GeV and $1 \leq Q^2 < 45$ $(\text{GeV}/c)^2$ in Fig. 47(b); the conclusion is essentially unchanged. For comparison, we show the expected ratio from Ref. 36 for $X_{BJ} = 0.1$ (dashed line) and $X_{BJ} = 0.3$ (dot-dashed line). The solid line shows the charge ratio measured in high-energy proton-proton interactions.[41] These data are much larger than the ratio measured in the present experiment.

The invariant distributions discussed above express the fragmentation function of the (ud) diquark into pions ($X_F < 0.0$) and the d quark into pions ($X_F \geq 0.0$). These fragmentation functions have been calculated neglecting quark spin effects[42] with the prediction that the invariant distributions expressed in the form

$$F(X_F) = A(1 - |X_F|)^n \tag{19}$$

should reflect favored and unfavored fragmentation. Thus, for $d \to \pi^-$, π^+, $n=1$ and $n=2$, respectively, while for $(ud) \to \pi^-$, π^+, $n=2$. In order to test this prediction, we exclude identified protons from the data sample and fit the invariant distribution to the equation (19) with the results given in Table II. While the results qualitatively agree with the predictions, the quantitative agreement is less good. Testing these predictions requires precise data at high $|X_F|$ and high W.

The fragmentation function for the (ud) diquark may also be expressed in the form $D(|X_F|) = (1/N_{ev})\, dN_T/d|X_F|$ for $X_F < 0$. This is shown in Figs. 48 and 49 for positive mesons (identified protons removed) and negative mesons, respectively, using events with $W \geq 4$ GeV and $1 \leq Q^2 < 45$ $(\text{GeV}/c)^2$. We also show for comparison the fragmentation function constructed by summing the corresponding distribution for $X_F \geq 0.0$ in $\bar{\nu}p$, from our experiment, and νp.[4] Such a construction, which would be appropriate if the u and the d quark fragmented independently, is a poor re-

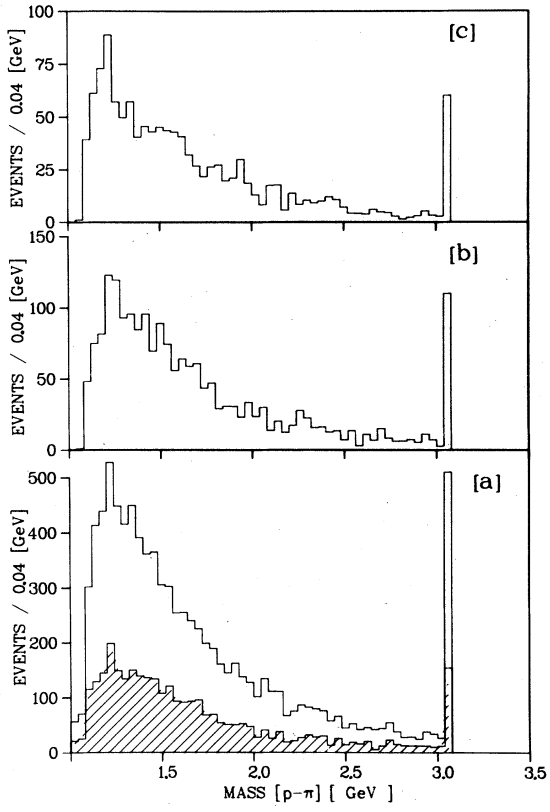

FIG. 53. The proton-pion effective mass in $\nu p \to \mu^- p \pi X$ events for (a) all combinations. Events with $X_{BJ} \geq 0.2$ are shown hatched, (b) all $\pi^+ p$ combinations with $X_F < 0$, and (c) all $\pi^- p$ combinations with $X_F < 0$.

presentation of the data.

In the deep-inelastic process, the d-quark and, presumably, the diquark fragmentation can result in resonances as well as the usual stable particles. In the "standard jet" model for quark fragmentation, specific assumptions are made regarding the fragmentation into resonances, and the inclusive ρ^0 production observed in this experiment agreed broadly with these assumptions.[43] The ρ^0 production was correlated with the current-quark fragmentation products. Baryons and baryon resonances are presumably more intimately connected with the target or diquark fragmentation.

The most obvious target fragment to look for is the proton itself. The distribution in X_F for those protons identified by either ionization or fitting is shown in Fig. 7. This distribution is biased since not all protons are detected, but even so, the proton and Λ^0 distributions of Fig. 7 are rather similar. Both depend on the (ud) core picking up a sea quark, u, or s, respectively. Proton production for $X_F \lesssim -0.5$ results mainly in protons identifiable by ionization and, in Fig. 50, we compare such proton production in $\bar{\nu}p$ reactions to similar νp data.[4] In each case, the distribution in $(1/N_{ev})dN_T/dX_F$ for events with $W \geq 4$ GeV is compared. The (uu) diquark system from the νp reaction is perhaps more efficient in producing protons with high momentum in the hadron c.m. system. Overall, there are 0.10 ± 0.01 (0.14 ± 0.01) identified protons per event in $\bar{\nu}p$ (νp) for $W > 4$ GeV.

The production of Λ^0 in $\bar{\nu}p$ and νp reactions[44] might be expected to differ significantly according to these simple ideas, and Fig. 51 shows that Λ^0 production is somewhat higher for the $\bar{\nu}p$ case at large negative X_F. No selection on W, Q^2, and X_{BJ} is made on either the νp or $\bar{\nu}p$ data. Since the mean value of W is higher for the νp than in the $\bar{\nu}p$ case, and since Λ^0 production increases with W, one would expect the νp rate to be about 40% larger than that for $\bar{\nu}p$ from this effect alone.

By similar arguments, the $\Delta^{++}(1236)$, which is a (uuu) state, is not expected to be seen in the $\bar{\nu}p$ process, where the core is (ud), although the $\Delta^0(1236)$ may be expected. The observation of $\Delta(1236)$ is complicated by the difficulty of identifying a sufficient fraction of the protons. In fact, in this analysis, unless definitely identified as a proton, all positive hadrons are tried both as proton and as π^+. The complete distribution in π-p mass, shown in Fig. 52(a), shows little evidence for Δ production. Requiring $X_{BJ} \geq 0.2$ to both enhance the valence-quark contribution and to suppress background does not improve the signal to noise for Δ as seen in the hatched histogram. If only $(p\pi)$ pairs with $X_F < 0$ are used, one sees no evidence for Δ^{++} in Fig. 52(b), but a small signal for Δ^0 is apparent in Fig. 52(c). In contrast, the production of both Δ^{++} and Δ^0 in νp interactions is larger as seen in Fig. 53, and this difference between $\bar{\nu}p$ and νp is reasonable in terms of the simple-minded quark transitions.

VII. SUMMARY

Some properties of the hadronic system in $\bar{\nu}p$ charged-current reactions have been presented. For the current-quark fragments, the predictions of the naive QPM in terms of the behavior of charge ratios, Z distribution, and mean transverse momentum are generally satisfied. After selections on W, Q^2, and X_F, the details of the quark jets are in reasonable agreement with the predictions of the standard jet model of Field and Feynman. No outstanding differences are observed between the properties of the quark and those of the diquark systems for the range of W and Q^2 available in our experiment.

ACKNOWLEDGMENTS

This experiment was made possible by the support of the Neutrino Department at Fermilab and, in particular, the operating crew of the 15-foot bubble chamber. We also wish to thank our scanners at all three institutions for their support. The help of J. J. Phelan in the early stages of the experiment is acknowledged. One of us (BM) wishes to gratefully acknowledge the collective wisdom of E. L. Berger, T. A. DeGrand, and T. Gottschalk. This work was supported by the U. S. Department of Energy.

---

*Present address: CERN, EP Division, Geneva 23, Switzerland.

†Present address: Bell Telephone Laboratories, Naperville, IL 60540.

‡Present address: U. S. Department of Energy, Washington, D.C. 20545.

§Present address: Fermi National Accelerator Laboratory, Batavia, IL 60510.

¶Present address: Department of Physics, University of Toronto, Toronto, Ontario M5S 1A7, Canada.

**Present address: Lawrence Livermore Laboratory, University of California, Livermore, CA 94550.

††Present address: Argonne National Laboratory, Argonne, IL 60439.

[1] R. P. Feynman, *Photon-Hadron Interactions* (Benjamin, New York, 1972).

[2]M. Derrick *et al.*, Phys. Rev. D 17, 1 (1978).
[3]P. C. Bosetti *et al.*, Nucl. Phys. B149, 13 (1979).
[4]J. Bell *et al.*, Phys. Rev. D 19, 1 (1979).
[5]N. Schmitz, in *Proceedings of the 1979 International Symposium on Lepton and Photon Interactions at High Energies, Fermilab*, edited by T. B. W. Kirk and H. D. I. Abarbanel (Fermilab, Batavia, Illinois, 1980), p. 379.
[6]L. M. Sehgal, in *Proceedings of the International Symposium on Lepton and Photon Interactions at High Energies, Hamburg, 1977*, edited by F. Gutbrod (DESY, Hamburg, 1977).
[7]G. Drews *et al.*, Phys. Rev. Lett. 41, 1433 (1978).
[8]R. D. Field and R. P. Feynman, Nucl. Phys. B136, 1 (1978).
[9]J. F. Martin *et al.*, Phys. Rev. D 20, 5 (1979).
[10]S. J. Barish *et al.*, Phys. Rev. D 18, 2205 (1978); E. Fernandez, A. Garfinkel, and A. T. Laasanen, Purdue University Report No. PU79-480 (unpublished).
[11]M. Derrick *et al.*, Phys. Rev. D 18, 7 (1978).
[12]E. Fernandez, Ph.D. thesis, Purdue University, 1980 (unpublished).
[13]E. Fernandez *et al.*, Phys. Rev. Lett. 43, 1975 (1979).
[14]S. J. Barish *et al.*, Phys. Lett. 91B, 161 (1980).
[15]J. Erwin *et al.*, Phys. Rev. Lett. 33, 1443 (1974).
[16]B. Musgrave, in *Neutrino '79*, proceedings of the International Conference on Neutrinos, Weak Interactions, and Cosmology, Bergen, Norway, 1979, edited by A. Haatuft and C. Jarlskog (Univ. of Bergen, Bergen, 1980), p. 556; M. Derrick *et al.*, Phys. Lett. 91B, 470 (1980).
[17]M. Pratap *et al.*, Phys. Rev. D 19, 1955 (1979).
[18]Our measurement of the proton multiplicity is 0.53 ± 0.15 as reported in Ref. 2.
[19]V. Blobel *et al.*, Nucl. Phys. B69, 454 (1974).
[20]L. S. Osborne, Phys. Lett. 63B, 456 (1976).
[21]M. Derrick *et al.*, Phys. Lett. 88B, 177 (1979).
[22]Ch. Berger *et al.*, Phys. Lett. 81B, 410 (1979).
[23]P. M. Stevenson, Nucl. Phys. B156, 43 (1979).
[24]R. Brandelik *et al.*, Phys. Lett. 89B, 418 (1980).
[25]R. Brandelik *et al.*, DESY Report No. 77/11, 1977 (unpublished).
[26]J. Bletschau *et al.*, Phys. Lett. 87B, 281 (1979).
[27]E. L. Berger, Z. Phys. C 4, 289 (1980).
[28]M. Haguenauer *et al.*, Report No. CERN/EP/80-124, 1980 (unpublished).
[29]M. G. Albrow *et al.*, Nucl. Phys. B160, 1 (1979).
[30]R. P. Feynman *et al.*, Phys. Rev. D 18, 3320 (1978); M. Gluck and E. Reya, Nucl. Phys. B145, 24 (1978); M. Gronau and Y. Zarmi, Phys. Rev. D 18, 2341 (1978); A. Mendez, Nucl. Phys. B145, 199 (1978); G. Altarelli and G. Martinelli, Phys. Lett. 76B, 89 (1978); A. Mendez *et al.*, Nucl. Phys. B148, 499 (1979).
[31]P. Mazzanti *et al.*, Phys. Lett. 81B, 219 (1979); G. Altarelli, in *Gauge Theories and Leptons*, proceedings of the XIII Recontre de Moriond, 1978, edited by J. Trân Thanh Vân (Editions Frontières, Gif-sur-Yvette, 1978), p. 398.
[32]C. K. Chen, Nucl. Phys. B133, 13 (1978).
[33]J. F. Martin *et al.*, Phys. Rev. D 20, 5 (1979).
[34]H. Georgi and H. Politzer, Phys. Rev. Lett. 40, 3 (1978).
[35]R. N. Cahn, Phys. Lett. 78B, 269 (1978).
[36]H. Deden *et al.*, Nucl. Phys. B181, 365 (1981).
[37]T. Kitagaki *et al.*, Phys. Lett. 97B, 325 (1980).
[38]T. A DeGrand, Phys. Rev. D 19, 1398 (1979).
[39]B. Andersson *et al.*, Phys. Lett. 69B, 221 (1977).
[40]T. Kafka *et al.*, Phys. Rev. D 16, 1261 (1977).
[41]J. R. Johnson *et al.*, Phys. Rev. Lett. 19, 1173 (1977).
[42]R. Blankenbecler and S. J. Brodsky, Phys. Rev. D 10, 2973 (1974); J. F. Gunion, *ibid.* 10, 242 (1974); G. R. Farrar, Nucl. Phys. B77, 429 (1974); R. Blankenbecler, S. J. Brodsky, and J. F. Gunion, Phys. Rev. D 12, 3469 (1975).
[43]M. Derrick *et al.*, Phys. Lett. 91B, 307 (1980).
[44]J. P. Berge *et al.*, Phys. Rev. D 18, 1359 (1978).